Advanced multiscale modal and frequency analysis of swirling spray flame near to lean blowout

Maria Grazia De Giorgi [a],[*], Pasquale Di Gloria [a], Donato Fontanarosa [b],
Antonio Ficarella [a]

[a] *Dep. of Engineering for Innovation, University of Salento, Via per Monteroni, Lecce, I-73100, Italy*
[b] *Dept. of Mechanical Engineering, KU Leuven, Celestijnenlaan 300A Postbus 2421, B-3001, Heverlee, Belgium*

A B S T R A C T

This study provides an in-depth characterization of Jet-A1 swirled flames' dynamics using advanced decomposition techniques on high-speed OH* chemiluminescence images. Research conducted in a 300-kW combustor with global fuel-to-air ratios $\Phi = 0.36$, 0.24, and 0.18 reveals dominant low-frequency components under ultra-lean conditions through statistical and wavelet analyses. Integrating Proper Orthogonal Decomposition (POD), Dynamic Mode Decomposition (DMD), and Multiscale Proper Orthogonal Decomposition (mPOD) enhances understanding by detailing the energy and frequency of flame modal structures. Observations show that as Φ decreases, flame size and intensity reduce, while fluctuations increase, indicating a transition towards unstable combustion dynamics. Furthermore, the frequency and intensity of burst phenomena increase, particularly in higher modes, indicating the system's approach to lean blowout (LBO). The application of nonlinear time series analysis, including autocorrelation (AFC) and phase space reconstruction, to mPOD eigenvalues, detects early warning signs of LBO. At lower Φ, the ACF reveals significant and frequent bursts, indicating high instability and intermittent behavior. Phase space reconstruction shows distorted orbits with a spiral-like structure, characteristic of substantial damping and irregular behavior near blowout conditions.

1. Introduction

Lean Blow Out (LBO) represents a considerable safety concern in aircraft engines, characterized by combustion instability when the air-to-fuel mixture becomes excessively lean. In this condition, the air-fuel ratio is too high, leading to flame oscillation that can jeopardize the safety of the combustor and the overall system. Understanding the lower stability limits of the combustor in proximity to LBO is vital for ensuring safe operation and preventing hazardous situations. Predicting LBO mechanisms is a complex task, as it defies easy simplification. Nassini et al. [1] have presented a Computational Fluid Dynamics (CFD) methodology that accurately describes and captures the dynamics of flame extinction under extremely lean operating conditions in gas turbine combustors. The methodology underwent initial validation using a laboratory test case. Sun et al. [2] performed an investigation using a semi-empirical correlation to quickly forecast the LBO limits. They used the Flame Volume model for a multi-point lean direct injection combustor with a unique dome geometry different from conventional combustors. In their study, Panchal et al. [3] used Large Eddy simulation to predict LBO in a rig combustor. They simulated the flame for different reductions in fuel flow rate while considering two different fuels. By analyzing

---

the combustion mode, they observed that the heat release rate (HRR) decreases with the equivalence ratio and is related to the non-premixed segment of the flame. De Giorgi et al. [4] conducted an experimental investigation that varied the fuel-to-air ratio of a burner until ultra-lean conditions were reached. They observed the presence of flame instabilities that had a negative impact on combustion efficiency. OH* chemiluminescence visualization helped in the study of the instability. The same authors [5], also, carried out an experimental investigation of the viability of high-speed visualization methods for combustion flames, and obtained significant parameters for the characterization of instability and subsequent blowout. Zhao et al. [6] aimed to comprehend the lower stability thresholds of gas turbine burners and the flame spray characteristics near LBO. Their goal was to assess how decreasing fuel rates and injector pressure drop affect LBO performance in a multi-staged vortex burner with an air-blast injector. Early detection of LBO is thus crucial for implementing preventive measures. Jin Jang et al. [7] evaluated a remote sensing method for dynamically measuring pressure in a combustion chamber, avoiding direct exposure of sensors to hot gases. Feasibility was verified through an acoustic experiment in a model gas turbine, evaluating sensor adapter performance. Modal shapes at a resonant frequency of 160 Hz were observed in various measurement positions. In an adapter performance experiment, the optimal design shape was determined, indicating improved accuracy in dynamic pressure measurements and a reduced risk of combustion instability. Zheng et al. [8] provided valuable results to assist in future fuel optimization and mitigate the risk of adverse performance from new fuels in gas turbines. They examined the effect of various alternative jet fuels with differing chemical and physical properties on the LBO limit. The ignition and LBO were experimentally investigated by Zhang et al. [9] under sub-atmospheric conditions in a combustor utilizing flame stabilization through trapped vortices. They highlighted a significant decrease in performance and, with the aid of high-speed images, captured the ignition process, revealing that the pilot flame rotates along with the main vortex. Raju Hasti et al. [10] introduced a data-driven approach employing machine learning to detect early signs of LBO in a real gas turbine combustor. They demonstrated this method using temperature and hydroxyl radical mass fraction (OH*) data obtained from large eddy simulations of Jet-A combustion.

The work conducted by Begiashvili et al. [11] presents a detailed analysis comparing various modal decomposition techniques, such as POD, DMD, and mPOD. Through the examination of four fluid dynamics test cases, they evaluate the performance of these techniques to provide a fair comparison and determine the most suitable solution for specific situations.

The Proper Orthogonal Decomposition (POD) is extensively employed in post-processing analysis of image datasets to extract essential information about flame dynamics overcoming limitations associated with traditional point-based measurement techniques. By enabling a full-field analysis, POD can identify dominant modes of variation within the data, facilitating a deeper understanding of complex, transient, and turbulent behaviors inherent in combustion processes. This approach is employed in the examination of combustion instabilities within gas turbine engines, offering valuable perspectives on sophisticated non-intrusive diagnostic methodologies for foundational research (Ruan et al. [12]). Charalambides et al. [13] applied POD to analyze flame chemiluminescence images generated by a Homogeneous Charge Compression Ignition (HCCI) engine and identified multiple ignition sites in each POD mode. Zao et al. [14] examine the influence of pilot swirlers on flame and thermo-acoustic instability in triple-swirler staged combustors. Utilizing POD, they identify energetic modes in velocity and OH radical fields. Increased swirl in the inner pilot swirler enhances vortex shedding and radial flame propagation, while swirl in the outer pilot swirler primarily affects vortex shedding. The energy ratio shows a nonlinear increase with swirl augmentation, emphasizing the significance of POD technique in a detailed analysis of these phenomena. Zhaoyi et al. [15] devised a sensor placement approach that optimizes monitoring efficiency while reducing implementation costs by integrating a reduced order model; they achieve this by decomposing the spatio-temporal field to be monitored using the POD method. An experimental investigation was carried out by Liu et al. [16] on the nonlinear response of a low-swirl, acoustically excited, premixed methane/air flame, and the results were visualized using POD to pinpoint the predominant structures within the flame characterized by the most energetic modes. Fontanarosa et al. [17] and De Giorgi et al. [18] conducted a study to assess the effect of emulsified fuels with added water and urea on combustion performance and pollutant emissions, considering various concentrations and equivalence ratios. Using POD on flame images (both broadband and chemiluminescence of the hydroxyl radical), they were able to identify the most crucial flame structures.

LBO can be studied by coupling Dynamic Mode Decomposition (DMD) to POD; in fact, Cao et al. [19] utilized high-speed OH laser-induced fluorescence measurements to capture dynamics like local extinction and reignition in a near-LBO flame. By employing POD and DMD, they analyzed the dynamics of the flame. The results indicated that in a stable flame, the radial vibration mode prevails, whereas the rotational mode is present in a near-LBO flame. Rajasegar et al. [20] used DMD to analyze the flame dynamics and provide a characterization by exploring the coherent structures and their energy contents. They utilized numerically generated images and OH-planar laser-induced fluorescence for this purpose. Weixuan et al. [21] used both POD and DMD analyses to investigate combustion instability in a solid-fuel ramjet combustor. The objective was to illuminate the flow characteristics and energy distribution among unstable self-modes. Palies et al. [22] employed the DMD technique to visualize the flow field and analyze temporal signal traces, aiming to investigate the mechanism responsible for the lean blowoff of a premixed flame. Nanda et al. [23] analyzed OH chemiluminescence data using POD and DMD in a multi-stage direct-injection multi-nozzle combustor. They employed unstable modes to identify the progression of combustion instability when different fuel stages interacted. Palies et al. [24] utilized images of a pre-mixed flame from a low swirl injector at three different equivalence ratios to apply the DMD technique. This approach reveals the frequencies related to the spatial modes. Yang et al. [25] successfully predicted the temperature of a critical point (HST) and the distribution of winding temperatures within a few seconds. This was achieved using a novel method based on DMD.

Multiscale Proper Orthogonal Decomposition (mPOD) is a technique that aims to balance energy maximization and spectral purity by constraining the spectral content of its modes to predefined frequency bands. This approach allows for multi-resolution analysis, with the calculation of POD at each resulting scale. Another benefit of mPOD is dimensionality reduction as it identifies the dominant energy modes of the system, allowing for more concise description and isolation of noteworthy features. In their study, Mendez et al. [26] applied mPOD to time-resolved PIV measurements, achieving a balance between decomposition convergence and spectral purity

in a flow through a cylinder under both stable and changing conditions. The mPOD technique successfully identified beat phenomena in the wake of the stationary cylinder and discerned the transition between different steady-state regimes in the transient test case. The same authors [27] conducted a comparative analysis of mPOD against other techniques, including POD, DMD, and Spectral Proper Orthogonal Decomposition (SPOD). The evaluation focused on assessing feature extraction capability, residual decay concerning the number of modes, and time-frequency localization. In another study, Procacci et al. [28] utilized mPOD to explore the dynamics of the flow field in flames stabilized by a sand body, both in swirling and non-swirling configurations. They determined that mPOD was successful in discerning primary flow patterns within the velocity field and isolating coherent structures associated with various instabilities in the flow.

Chemiluminescence is an important spontaneous emission from flames that can be used to study combustion and asses its characteristics. Wenkai et al. [29] investigated OH* chemiluminescence as a valuable indicator for analyzing the rate of heat release in flames. Lean combustion is advantageous for reducing NOx emissions, but it is prone to instability, and accurately measuring the equivalence ratio in real-time is a crucial goal. On a lean premixed dual-swirl flame, Liu et al. [30] investigated the characteristics of methane combustion, temperature, and radical concentration for NOx emissions, as well as chemiluminescence, by varying equivalence ratios (Φ) and swirl numbers (S). They observed that Φ and S have distinct effects on chemiluminescence intensities and flame structure. A linear relationship was proposed to monitor NOx emissions based on chemiluminescence. Tobias et al. [31] used OH* chemiluminescence images to detect reaction zones in a rotary detonation combustor (RDC), which has the potential to provide efficiency gains as a pressure-gain combustion system for gas turbine. Aradhey et al. [32] investigated the interactions between unreacted acoustics and spray droplets in fully self-excited combustion instabilities. They used OH* chemiluminescence imaging to analyze the flow field. In the investigation conducted by Zhao et al. [33], a burner was specifically crafted to produce axisymmetric diffusion flames, and chemiluminescence images of OH* were recorded from laminar hydrogen diffusion flames.

The authors of this work conducted an experimental investigation of the mPOD technique using OH* chemiluminescence images, starting from pressure signals up to the use of the POD technique. Specifically, three conditions of the global equivalence ratio (Φ) were studied in a combustor that is a 300 kW liquid-fuel single swirl cylindrical burner, designed with inspiration from a typical aeroengine gas turbine configuration to characterize lean combustion conditions: $\Phi = 0.36$, $\Phi = 0.24$, and $\Phi = 0.18$. Experimental tests were carried out using the burner in non-premixed fueling mode, pressure signals were acquired for the two extreme cases of the global equivalence ratio ($\Phi = 0.36$ and $\Phi = 0.18$) and the data generated by it were studied through the Fast Fourier Transform (FFT). Flame stability characterization was carried out by chemiluminescence of the OH* species, obtained from images acquired through a fast camera equipped with a photographic filter.

Early detection of the system approaching blowout is crucial to prevent the occurrence of blowout phenomena and to increase the stability margin by taking necessary measures in widely used turbulent combustors. To achieve this, it is essential to analyze the characteristics of combustor dynamics leading up to blowout. In the present work, the analysis of the presence of flame intermittency states, based on the temporal series of the mPOD eigenvalues, has been conducted to identify the approach of blowout.

The mPOD emerges as a particularly methodology for the characterization of Lean Blowout (LBO), a critical phenomenon characterized by the intricate interplay of multiple scales, ranging from large-scale flow structures crucial for air-fuel mixing to small-scale turbulence that significantly influences flame stability. The mPOD's inherent capability to segregate flow fields into distinct mode shapes, leveraging both spatial and temporal characteristics, provides an enhanced resolution that delineates these scales with exceptional clarity. Such refined separation is instrumental in deciphering the complex interactions that precipitate the onset of LBO, shedding light on the underlying mechanisms responsible for flame extinguishment.

As flame approaches LBO, it exhibits markedly unstable behaviors, often obscured by the experimental noise inherent in measurement setups. Here, the mPOD's advanced filtering prowess comes to the fore, adeptly isolating coherent structures from background noise, thereby ensuring that the analysis remains focused on the physical phenomena directly relevant to flame behavior near extinction. This capability is critical in accurately characterizing the precursors to flame extinction, offering insights into pertinent dynamic features crucial for understanding LBO dynamics.

The period leading up to LBO is typified by critical transitions, including shifts in dominant flow structures and emergent instabilities. The mPOD stands out by its capacity to distinctly identify and segregate modes across a spectrum of frequencies and energy levels, thus enabling a more nuanced detection of these transitional behaviors compared to methodologies like traditional POD or Dynamic Mode Decomposition (DMD). By spotlighting the dynamic alterations that herald LBO, mPOD furnishes early detection of shifts that signal critical thresholds in flame stability, providing a valuable framework for predicting and mitigating LBO scenarios.

The mPOD's adaptability allows for a focused analysis on the scales most pertinent to understanding the dynamics of LBO, tailoring the decomposition process to elucidate scales directly influencing flame stability and LBO mechanisms.

Moreover, the identification of dominant energy modes facilitated by mPOD provides a robust means to characterize the system's behavior while simultaneously achieving a reduction in data dimensionality. This aspect is particularly valuable for interpreting complex datasets and deriving meaningful conclusions about system dynamics.

Combustion dynamics are dominated by complex processes involving a significant level of determinism, especially under fuel-lean conditions. Recent experimental and computational studies on laminar burners have indicated that combustion systems can undergo secondary bifurcation to states such as frequency-locked, quasi-periodic, period doubling, intermittent, and chaotic oscillations [34, 35]. Practical combustors are inherently noisy, characterized by swirling turbulent flows, and they display intermittent oscillations under various operating conditions. These types of oscillations were investigated at the onset of combustion instabilities by Nair et al. [36].

However, no studies have been performed to characterize intermittency prior to blowout in a turbulent combustor. Therefore, it is of great importance to characterize the occurrence of intermittency in industrial combustors, which is a signature prior to flame

blowout, by applying the tools of dynamical systems theory.

In other works, the study of intermittency has been conducted by analyzing the time series of pressure signals. In the present work, we investigate the intermittency by analyzing the eigenvalues of the mPOD. This analysis focuses on identifying the approach of blowout by examining the presence of flame intermittency states based on the temporal series of the mPOD eigenvalues.

Despite the compelling advantages offered by mPOD in flame characterization, its application remains underexplored in the literature.

The novelty of the work lies in its integrated approach to analyzing flame dynamics using a combination of Proper Orthogonal Decomposition (POD), Dynamic Mode Decomposition (DMD), and multiscale POD (mPOD).

By combining the strengths of POD, DMD, and mPOD, the study offers a more comprehensive understanding of flame dynamics. This approach enables the examination of flames through different spatial—energy content with POD, frequency content with DMD, and a hybrid focus on both energy and frequency with mPOD. This multifaceted analysis provides a richer, more nuanced understanding of flame behavior than any single method could achieve on its own.

The work highlights the superiority of mPOD over traditional methods (POD and DMD) in efficiently correlating spatial structures of the flame with their respective frequencies. This efficiency is not just in computational terms but also in the depth of insights gained, particularly in understanding the dynamics and instability of flames. The ability of mPOD to discern between spatial structures' dynamics and associated frequencies marks a significant advancement in the field.

The integration of statistical and wavelet analysis of pressure signals with modal decomposition techniques and nonlinear analysis of mPOD eigenvalues allows for a detailed characterization of flame behavior under varying conditions. By employing autocorrelation and phase space reconstruction, this comprehensive approach captures temporal relationships, periodic behavior, and stability. It is particularly effective under lean and ultra-lean conditions, identifying key phenomena such as the dominance of low-frequency components and the transition towards more unstable combustion dynamics as the global fuel-to-air ratio decreases. This has implications for improving combustion efficiency and reducing emissions in swirling combustors.

The insights gained from mPOD analysis can be directly applied to develop more robust combustion control strategies. By understanding the specific modal interactions and burst dynamics that lead to LBO, control systems can be designed to counteract these instabilities, thereby enhancing the reliability and efficiency of combustion processes.

2. Materials and methods

2.1. Combustion test facility and imaging methods

The experimental investigation took place at the Green Engine laboratory, University of Salento, in Lecce, Italy. The test rig (a 300-kW swirled liquid-fueled combustor) consists of a cylindrical combustion chamber with an inner diameter equal to 4 cm and a length of 29 cm. A sketch is shown in Fig. 1: an external compression system equipped with resistive pre-heater supplies the overall air flow, this involves the introduction of the substance into the combustion chamber through two separate flow rates via two concentric annular tubes. The internal tube is furnished with an eight-septa, 45° swirler, as illustrated in Fig. 2. The liquid fuel (Jet-A1) is fed at 7 bar using a fuel pump AUDI 8K0.906.095.B Pierburg 7.50103.00, and it is sprayed into the combustion chamber with a Monarch single-hole nozzle (Monarch 1.20 45° R), which features a 45° injection angle. The primary air flow rate is 91.5% of the total air flow rate, while the remaining 8.5% enters the combustion chamber axially. The fuel mass flow rate was gauged using the VSE EF 0.04 ARO 14 V PNP/2 flow meter, with an accuracy of ±2% of the reading. The air mass flow rate was approximated by measuring the volumetric
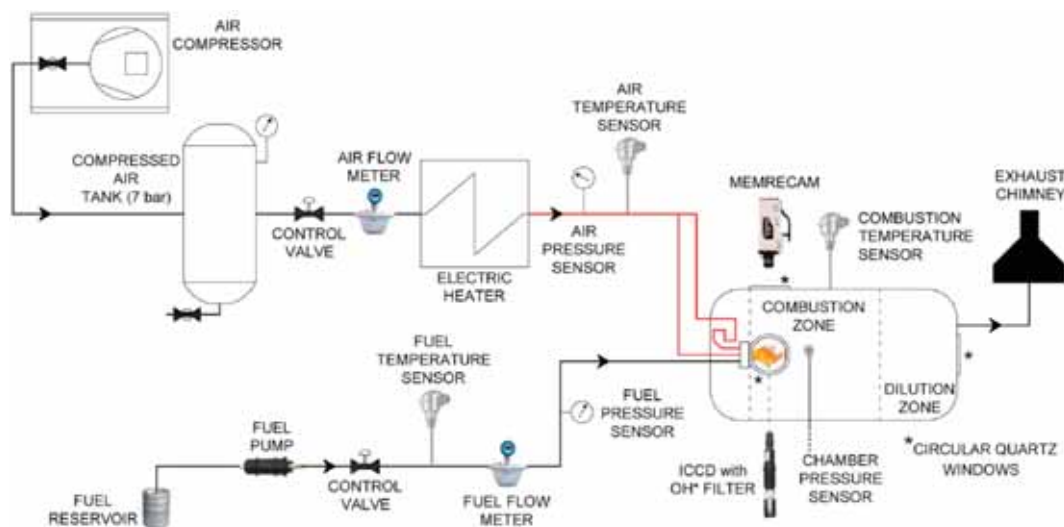

Fig. 1. Green Engine combustion chamber set-up diagram. (For interpretation of the references to color in this figure legend, the reader is referred to the Web version of this article.)
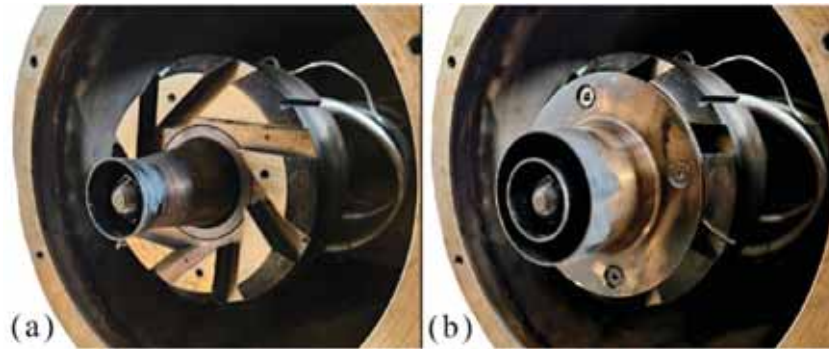
Fig. 2. Detail of the burner eight-septa, 45° swirler with fuel nozzle in the center without (a) and with (b) mounting seal plate.

flow rate of air under standard conditions using the Asa-C6-3100/38/EX1 asameter (accuracy: ±1% f.s.v.). This value was then adjusted based on the air inlet pressure, determined by a pressure transmitter with a ceramic sensor model Nuova Fima ST18, boasting an accuracy of ±0.75% f.s.v., and temperature.

Concerning the diagnostic equipment, combustion chamber pressure was monitored with the Kistler PiezoSmart Type 4045A2 pressure sensor located close to the flame in the combustion zone. This sensor was paired with the piezoresistive amplifier Type 4618A0, which has a pressure range of 0–2 bar. Pressure data were captured at a sampling rate of 10 kHz using a LabVIEW control and acquisition system from National Instruments. The pressure sensor was integrated into a cooling circuit, ensuring forced coolant circulation through a dedicated pump to maintain the local temperature below its maximum operating of 413 K. The optical access to the combustion chamber was ensured by two out of the three circular quartz windows; the first one with a perpendicular-lateral axis to the combustor axis, the second one with an upward-perpendicular axis, both located close to the fuel injectors, as depicted in Fig. 1. The first window was equipped with the ICCD camera Phantom M320S with a Lambert image intensifier, while the second window was outfitted with the Memrecam GX-1F camera from NAC Image Technology. A narrow-band filter was applied to the ICCD camera's lens to capture OH* radical emissions. For each test condition, 1000 images were captured at rate of 1000 Hz. Each image captured by the ICCD was 1574 × 966 pixels in the axial and radial directions respectively, which after the cropping operation produced an approximate field of view 60 × 56 mm. The intensifier gain for the OH* chemiluminescence recordings was configured at 900. The OH* filter, with a center at 307.1 nm, had a 10 nm bandpass and 68% transmittance. Meanwhile, each image acquired by the Memrecam had dimensions of 1280 × 1024 pixels. After the cropping operation, resulted in a field of view of approximately 45 × 56 mm.

Due to the non-axisymmetric nature of the air feeding line in the burner's geometry and potential slight movements of the flames during experimental measurements, the flame images obtained using the ICCD camera did not exhibit perfect axisymmetry.

A variety of statistical, spectral, and wavelet-based methods have been devised to establish correlations between extracted parameters and the physical properties characterizing unstable flames. Fig. 3 describes the workflow for flame monitoring, and Table 1 summarizes the applications of each data analysis technique. First, the OH* emissions images were captured by using high-speed digital imaging systems.

Fundamental combustion frequencies were obtained through the pressure signals data through FFT and Wavelet Decomposition techniques. Results were compared with characteristic frequency ranges found by POD analysis. Flame characteristics were then extracted from the images through POD techniques. This analysis to break down a sequence of experimental images (snapshots) into a collection of mutually orthogonal spatial modes, referred to as coherent structures. The meaning of these coherent structures, unlike that suggested by Ref. [37], is to refer to patterns of chemiluminescence intensity that are coherent both in space and time. These structures can highlight areas of high chemical activity or regions with significant fluctuations in heat release. Understanding these patterns provides insights into the stability and efficiency of the combustion process. These structures were then ranked according to their energy content using singular value decomposition (SVD).
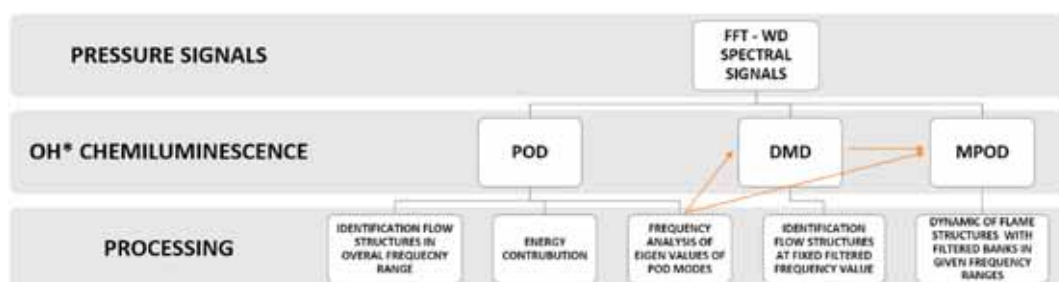

Fig. 3. Methodology applied for the study of combustion instability.

Table 1
Summary of the applications of each data analysis technique.

Data Analysis Technique	Dataset	Purpose
FFT	Pressure Signals	To identify dominant frequency components and their contributions to the pressure signals
POD	Luminance Images	To extract significant spatial modes and identify patterns in flame dynamics
FFT	POD Eigenvalues	To identify dominant frequency components and their contributions to the POD modes and choice the frequencies values for DMD and mPOD analysis
Wavelet Decomposition	Pressure Signals	To analyze the pressure signals at different scales and capture transient phenomena
DMD	Luminance Images	To capture dynamic modes and elucidate flame structures by filtering specific frequency bands
mPOD	Luminance Images	To enhance the analysis of flame dynamics by filtering specific frequency bands and identify flame structures at given frequencies evolving over time

It permits the extraction of the time-averaged (mean) heat release mode, as well as the high-frequency heat release fluctuation structures and their energy levels. Then DMD and mPOD analyses were performed based on the relevant frequency values identified by the FFT analysis of the eigenvalues of POD more energetic modes.

2.2. Flame image processing

2.2.1. Proper Orthogonal Decomposition

For every test case, the dataset comprised a series of $N_{img} = 1000$ greyscale images. Each pixel in the images was represented by an 8-bit discretized grey level value ranging from 0 to 255, denoting complete darkness (ultra-low brightness) to complete brightness (ultra-high brightness), respectively. MATLAB software, equipped with custom routines, was employed to process the image set. A cropping operation using an appropriate window was applied to display the images. The grayscale of the images was then converted to luminance I, which ranged between 0 and 1. The time-average image $\bar{I}\left(x_i, y_j\right)$ at a specific pixel point $P\left(x_i, y_j\right)$ was calculated, as well as the time variance image at each pixel point was computed. Using the reconstructed time-averaged image, the time variance image was calculated at each pixel point using in Eq. (1):

$$S_I^2\left(x_i, y_j\right) = \frac{1}{N_{img} - 1} \sum_{k=1}^{N_{img}} \left| I\left(x_i, y_j, t_k\right) - \bar{I}\left(x_i, y_j\right) \right|^2 \tag{1}$$

where t_k represents the k-th instant of ranging from 1 to N_{img}, and $\left(x_i, y_j\right)$ denotes the pixel row and column indices denoting point P in the image.

The luminance of an image functions as a comparative indicator of the electromagnetic radiation emitted by the flame. Consequently, higher heat release during combustion leads to a higher flame temperature and increased image luminance. The information within the image luminance facilitates extrapolation of pertinent observations on average flame structure in terms of extension, shape, and emission intensity, associated with the average image luminance map $\bar{I}$. Conversely, image luminance variance S_I^2 accounts for local fluctuations in flame emissions, providing valuable insights into the spatial distribution and extent of these fluctuations. Specifically, more unstable flame behavior corresponds to more fluctuating emission fields, resulting in an increase in image luminance variance, as discussed in the subsequent section 3.2.

The Proper Orthogonal Decomposition technique was then used for high-speed image acquisitions to perform a space-time modal characterization of flame behavior. This technique, detailed by Sirovich [38] and Tropea et al. [39], extracts an orthogonal basis of eigenvalues from the flow data field $g(x; t)$, separating spatial and temporal contributions:

$$g(x;\ t) = \Sigma_i\ g_i(x;t) = \Sigma_i\ a_i(t)\ \varphi_i(x) \tag{2}$$

here, $a_i(t)$ represents the i-th temporal eigenfunction, capturing information about the dynamics of modal coherent structures, and $\varphi_i(x)$ describes the i-th spatial eigenfunction—a flow image capable of capturing sizes and forms of modal coherent structures, with x representing generic spatial coordinates. The energy contribution of the image relative to the i-th POD mode is:

$$\Lambda_i = \frac{\lambda_i}{\Sigma_{j=1}^{N_{POD}}\ \lambda_j} \tag{3}$$

with λ_i being the i-th eigenvalue of the data autocorrelation tensor.

There are two strategies that can be utilized with the POD technique, grounded on the combination of average and correlation, as described by Kypraiou et al. [40]. The first is the classical or direct method by Lumley [41], relying on spatial correlation and temporal average. The second, applied in this work to describe the flame dynamics, is the snapshot method of Sirovich [38], which utilizes spatial average and temporal correlation, making it particularly suitable for datasets with high spatial resolution but a brief time history. Certainly, the dimension of the eigenvalue problem is determined by the number of snapshots of the dataset, where in this case, $N_{POD} = N_{img}$.

2.2.2. Dynamic Mode Decomposition

A matrix is constructed from the set of N images of OH* chemiluminescence. The DMD provides a low-dimensional representation in a vector space generated by the bases of the POD; specifically, two matrices are obtained: A_0 and A_1, which consist of sequences of images from 0 to $N-1$ and from 1 to N, respectively. From the matrix J of POD modes, the conjugate transpose J^* is obtained through an SVD of the matrix of the chemiluminescence image set A_0.

The DMD matrix H_{DMD} will, therefore, be determined by minimizing the Frobenius norm of the difference between A_1 and JYJ^*A_0:

$$H_{DMD} = J^* A_1 R Y^{-1} \tag{4}$$

where R represents a matrix containing information about the spatiotemporal modes of the image set, Y is a diagonal matrix determined by the non-zero singular values of A_0, and Y^{-1} is its respective inverse [42].

2.2.3. Multiscale Proper Orthogonal Decomposition

The technique described in this paragraph is the one of most interest for the analysis for this work. Multiscale Proper Orthogonal Decomposition (mPOD) joins multiresolution analysis (MRA) with a standard POD to reach a compromise between convergence decomposition and spectral purity of the resulting modes [26]. Applying MRA, the mPOD divides the correlation matrix into segments that represent various scales while retaining non-overlapping sections of the correlation spectra. With POD, mPOD then derives the most efficient basis from each of these scales. Exploring the impact of temporal filtering on the dataset's frequency content becomes intriguing. Specifically, the focus is on a series of filters designed to isolate specific segments of the frequency spectra. The filter bank includes a low-pass filter, a high-pass filter, and a band-pass filter. The entire post-processing phase has been studied using user-defined routines customized with MATLAB software.

It is important to note the filtering procedure and the underlying theory of the suggested mPOD. When addressing frequency domain filtering, this procedure is executed through a straightforward multiplication, represented in matrix notation as the Hadamard product. The first step of the mPOD algorithm is to assemble the matrix of data collecting the set of temporal realizations (snapshots):

$$D[i,k] = [d_1[1] \ \ldots \ d_k[1] \ \ldots \ d_{n_t}[1] \vdots \ldots \vdots d_k[n_s] \vdots \cdots \vdots d_{n_t}[n_s]] \tag{5}$$

where $d_k[i]$ is a column vector of each snapshot. The second step involves calculating the temporal correlation matrix K and its Fourier transform $\widehat{K}$ from:

$$\widehat{K} = \overline{\psi_F} K \overline{\psi_F} \Leftrightarrow K = \psi_F \widehat{K} \psi_F \tag{6}$$

where $\overline{\psi_F}$ is the DFT temporal structure. After analyzing the frequency content within the correlation spectra $\widehat{K}$, the subsequent step entails delineating the frequency division vector F_V and forming the collection of corresponding transfer functions. This choice represents a pivotal stage, setting the spectral constraints for the mPOD mode. Each mode exhibits a unique development of spatial and temporal structure and holds the potential to capture the essential characteristics of some data. The frequency division was defined by the user after interpreting the POD results. The final step involves completing the decomposition through projection and normalization as described in Eq. (7):

$$\theta \Omega = D(\psi^T)^{-1} = C \to \theta = C \Omega^{-1} \tag{7}$$

and in particular θ is the spatial structure, $\Omega = diag[\sigma_1, \sigma_2, \ldots, \sigma_{rk(D)}]$ is diagonal matrix that includes the energy contribution of each mode, $D = \theta \Omega \psi^T$, ψ represents the temporal structure and C is matrix $C = D(\psi^T)^{-1}$ [43].

2.3. Wavelet decomposition

A more advanced version of Fourier analysis can be considered the wavelet transform. This technique can have an adjustable time range, with small ranges at high frequencies and large ranges at low frequencies. The wavelet transform is the time-frequency interpretation of non-stationary signals. Through distinct components, with a low time resolution, the signal is decomposed. The term 'details' (d) refer to the low time-scale signal and the high-frequency components. The detail component d_1 refers at the uppermost frequency range, while the detail component d_2 is the next highest frequency band that has half the bandwidth of d_1, and so on. Using this technique, the pressure signals were decomposed into nine levels and a Daubechies [44] order 2 wavelet was used as the mother wavelet.

The decomposition levels were: d_1 = 2500–5000[Hz], d_2 = 1250–2500[Hz], d_3 = 675–1250 [Hz], d_4 = 312.5–675 [Hz], d_5 = 156.3–312.5 [Hz], d_6 = 78.1–156.3 [Hz], d_7 = 39.1–78.1 [Hz], d_8 = 19.5–39.1 [Hz], d_9 = 0–19.5 [Hz].

The selection of 9 levels of decomposition was driven by the intrinsic frequency content of the pressure signals we analyzed. These signals contain fluctuations that span a wide range of frequencies, and it is essential to choose a level of decomposition that allows for a detailed examination of the signal across these frequencies. The 9th level was determined to be particularly effective in resolving the critical frequencies associated with the dynamics of interest, such as those related to combustion instabilities.

The energy content of the individual components of the decomposed signal can be examined. Specifically, assuming E_j represents the wavelet energy of the decomposed magnitude signal, the probability distribution of the energy for each magnitude is defined by the following formula:

$$P_j = \frac{E_j}{\sum_{j=1}^{9} E_j} \tag{8}$$

where E_j is defined as the summation of the squared detailed coefficients of the wavelet transform, d_j:

$$E_j = \sum_k |d_j(k)|^2 \tag{9}$$

Another variable that could be studied is the wavelet entropy [45]. This method is valuable for estimating the complexity of a random signal by quantifying the unknown degree of a sequence. In this work, Shannon entropy [46] will be employed. Shannon's entropy is represented as follows:

$$S = -\sum_{j=1}^{9} p_j \ln \ln p_j \tag{10}$$

2.4. Test conditions

Using pre-heated inlet airflow at a temperature $T_{a,in}$ equal to 410 K, experiments have been conducted by controlling the air mass flow rate at 40 $\frac{g}{s}$, 60 $\frac{g}{s}$ and 80 $\frac{g}{s}$ respectively and maintaining a steady fuel mass flow rate at 1.00 $\frac{g}{s}$. This resulted in three different

equivalence ratios near to the LBO, i.e. 0.36, 0.24 and 0.18, which were determined as $\Phi = \dfrac{\left(\frac{\dot{m}_f}{\dot{m}_a}\right)}{\left(\frac{\dot{m}_f}{\dot{m}_a}\right)_{st}}$ where $\dot{m}$ represent the mass flow rate

and the subscripts f and a denote the fuel and the air flows, while st indicates the stoichiometric conditions with the stoichiometric fuel-to-air ratio of 14.5. The blow out boundary conditions are 130 $\frac{g}{s}$ obtaining an equivalence ratio of 0.11. The fuel-air distribution within the combustor is not spatially uniform; therefore, the equivalence ratio should be understood as the global fuel-air ratio.

3. Results

The thorough analysis of results is subdivided into five sections. The first section (Sec. 3.1) deals with the frequency analysis of the pressure signals for the highest and lowest Φ test cases (0.36 and 0.18), aiming to characterize their frequency content. The next section (Sec. 3.2) presents the statistical characterization of the flame regimes for all three cases ($\Phi = 0.36$, $\Phi = 0.24$ and $\Phi = 0.18$) in terms of instantaneous flame dynamics, mean and variance maps of the chemiluminescence emission in the OH* spectrum, obtained by intensified high-speed acquisitions. In the third section (Sec. 3.3), some aspects of the flame instability of the OH* spectrum are preliminarily analyzed through the Proper Orthogonal Decomposition (POD) technique, and it is explained the strategy used to determine the frequency filters used in the mPOD analysis in Sec. 3.5. In Section 3.4 the same image dataset is processed by applying the Dynamic Mode Decomposition (DMD) and the modal structures corresponding to the peaks of the most relevant POD frequencies. Finally, in the last section (Sec. 3.5), the flame dynamics characterization resulting from the mPOD analysis is presented and discussed, and the most important insights are highlighted.

3.1. Combustion signal of Jet-A1 fuel: pressure signal

In this first subsection, the pressure inside the combustion chamber is analyzed for the for the highest and lowest Φ test cases (0.36 and 0.18), Fig. 4 shows the original pressure signals recorded at 10000 samples per second. Frequency analysis was performed by applying the Fast Fourier Transform (FFT) to both reactive flame pressure signals and non-reactive flame pressure signals. As highlighted in Fig. 5, the non-reactive flame yields no contribution for both cases except for negligible peaks attributed to the system's power supply current. Moreover, the most relevant frequencies for reactive flames fall within the range the range below 50 Hz, with a decreasing peak of about 47% when operating under ultra-lean conditions.
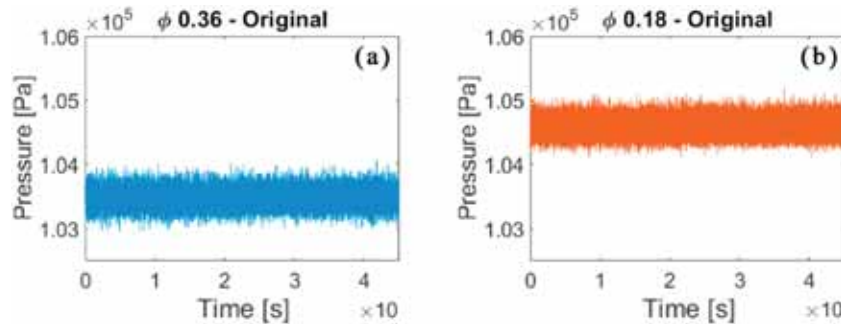

Fig. 4. Original pressure signal for the highest and lowest Φ test cases: $\Phi = 0.36$ (a) and $\Phi = 0.18$ (b).
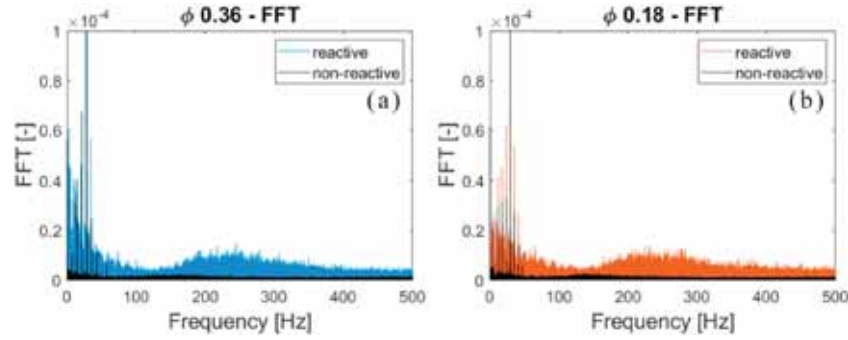
Fig. 5. FFT of the pressure signal for two test cases compared with a non-reactive flame: $\Phi = 0.36$ (a) and $\Phi = 0.18$ (b).

The analysis of the pressure signals has been extended by computing the Wavelet Decomposition. Fig. 6 exhibits the root mean square (RMS) of the resulting wavelet components (RMS_{wd}). Fig. 5 shows that most of the fluctuation content is present in the first two frequency ranges (0–19.5 Hz and 19.5–39.1 Hz) and, at frequencies higher than 150 Hz, the fluctuations are less relevant. The observations made for Figs. 5 and 6 confirm the choice to study the subsequent frequency domains up to 150 Hz and the choice of filters applied for mPOD, which will be discussed in Sec. 3.3. Fig. 6(b) shows the ratio between RMS_{wd} in the indicated frequency bands and the value in the range [0–19.5 Hz], which is the band of approximation component, for both operating conditions. The value assumed by this ratio is higher at $\Phi = 0.18$ than $\Phi = 0.36$. In the range [19.5–31.1] Hz the dimensionless RMS increases by 20% from $\Phi = 0.18$ to $\Phi = 0.36$. The same trend is also evident for the higher frequency bands. This confirms that by lowering Φ (leanest condition) the contributions of the detail components, which represent the fluctuations, become more relevant.

3.2. Combustion structure of Jet-A1 fuel: OH* chemiluminescence emissions

In this section, the immediate dynamics of the flame are depicted, encompassing an examination of both the average and variance in luminance. This analysis is derived from the high-speed visualization of the chemiluminescent flame, specifically focusing on the radical OH* emissions.

While the line-of-sight area measured from high-speed OH* chemiluminescence images may not precisely correspond to the actual flame area, it can still be used to qualitatively assess the overall flame fluctuation. This is because chemiluminescence images can reasonably represent the global flame shape to a considerable extent. The near-UV spontaneous emission from OH* is detectable solely in the heat release zone and is not observable in the region occupied by burned gases. A grayscale mapping technique was employed to portray the immediate flame dynamics, whereas a false-color mapping approach was utilized to illustrate the average and variance. Both color schemes are linked to the pixel signal's luminance, offering a purely visual depiction of the locations with the most significant relative intensities of the OH* chemiluminescence emission within the reaction zone. This, in turn, serves as a qualitative index of the localized heat release (HRR). The temporal variations in HRR pose potential challenges related to flame instability, as fluctuations in heat release over time can lead to significant issues. The most direct issue arising from HRR fluctuations is the combustion instability, which occurs when pressure waves within the combustion chamber interact with the flame in such a way that they reinforce each other. This can lead to oscillations that can grow to levels capable of damaging the combustion system. Variations in HRR can also lead to incomplete combustion resulting in increased emissions of unburned hydrocarbons (UHC), carbon monoxide (CO), and particulate matter. Temperature fluctuations associated with HRR variability can lead to increased NOx formation, which is temperature dependent. Fluctuations in HRR can affect the thermal efficiency of the combustion process as stable combustion typically allows for more complete and efficient fuel conversion, resulting in better fuel economy and lower operational costs. The fluctuations in chemiluminescence signal intensity primarily result from interactions between the flame and turbulence. They are closely associated
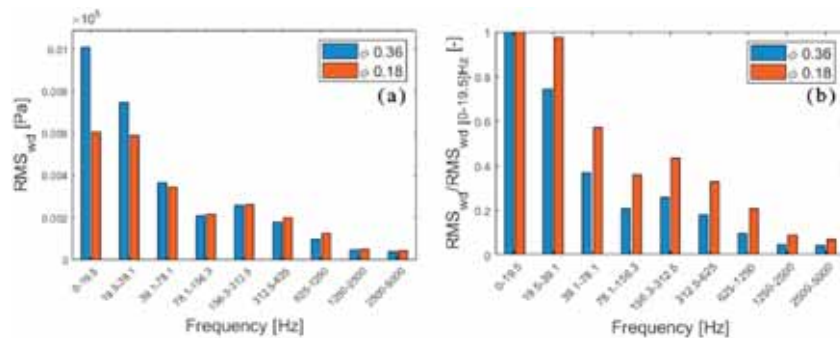

Fig. 6. Root Mean Square (RMS) of wavelet components for pressure signal for the highest and lowest Φ test cases: $\Phi = 0.36$ and $\Phi = 0.18$.: a) absolute pressure; b) dimensionless values with respect to the one in the range [0–19.5] Hz.

with the temporal variations in the heat release rate, presenting a potential source of serious flame instability problems.

Figs. 7–9 depict the momentary behavior of the flame at three distinct overall fuel/air ratios. To enhance the clearness of this paper, these acquisitions were chosen by excluding 10 consecutive frames from time-resolved measurements, and a circular quartz window was added relative to the nozzle. The area highlighted in red inside the circular quartz window represents the position of the nozzle. At $\Phi = 0.36$ the flame is raised, and the fluctuations in the reaction intensity are minimal within the chosen time frame. If the fuel-air ratio decreases, the flame progressively decreases in size and intensity, and fluctuations become more prominent. The images of the transitional case at $\Phi = 0.24$ indicate that the flame exhibits a back-and-forth propagation in the axial direction. At certain moments, the flame is observed to be connected to the nozzle exit, coinciding with a maximum intensity reaction zone located near the combustor wall, then partial flame fragments are often swept downstream with an incomplete burning of the fuel-air mixture. In a previous study [47], comparable flame behavior was identified, linking it to robust periodic interactions between vortices and the inner shear layer (ISL). This interaction results in substantial velocity oscillations in the jet regions. Close to the LBO condition, the flame edge extends nearer to the axis and the combustor nozzle.

Due to the turbulent characteristics of the swirled flow field and the random dispersion of fuel droplets, the flame morphology in the spray flame undergoes significant changes during the process of LBO, which includes the growth, splitting, and rotation of flame fragments. The movement of the high intensities OH* structures suggest a possible helical motion of the flame that will be confirmed by the modal decomposition analysis, and it is in agreement with previous studies [47], a zig-zag pattern of vortices was identified, suggesting the presence of a precessing vortex core (PVC). The PVC is distinguished by its helical, tornado-like rotational dynamics and is commonly observed in gas turbine combustors stabilized by swirl.

Fig. 10 displays the broadband average of the flame for three different global fuel/air ratios. Transitioning from $\Phi = 0.36$ to $\Phi = 0.18$, the intensity, size and symmetry of the flame gradually decrease, approaching closer to the nozzle exit.

Fig. 11 illustrates how the global equivalence ratio (Φ) influences the combustion of Jet-A1, resulting in varied sizes and shapes within the heat release zone and affecting the concentration of OH* radicals generated through chemical reactions in the flame.

Clear variations in OH* chemiluminescence levels are evident for each operating condition. A V-shaped flame, consistent with Φ values of 0.24 and 0.18, is observed, with the flame being attached to the nozzle exit. However, at $\Phi = 0.36$, the flame becomes detached. Notably, the asymmetry observed in the chemiluminescence fields is closely linked to the non-axially symmetric geometry of the swirl's feed duct. The swirled flows exhibit sensitivity to input conditions, and the asymmetry of the OH* images become more pronounced with decreasing Φ. Different flame zones are discernible based on the OH* levels. Regions lacking OH* (depicted in blue) indicate unburned gas mixed with adjacent burned gas. Areas with significant OH* levels (depicted in red) signify the presence of OH* formed in the reaction zones. Areas with moderate and low levels of OH* represent burned gas where the OH* concentration has diminished toward equilibrium as it moves away from the reaction zone.
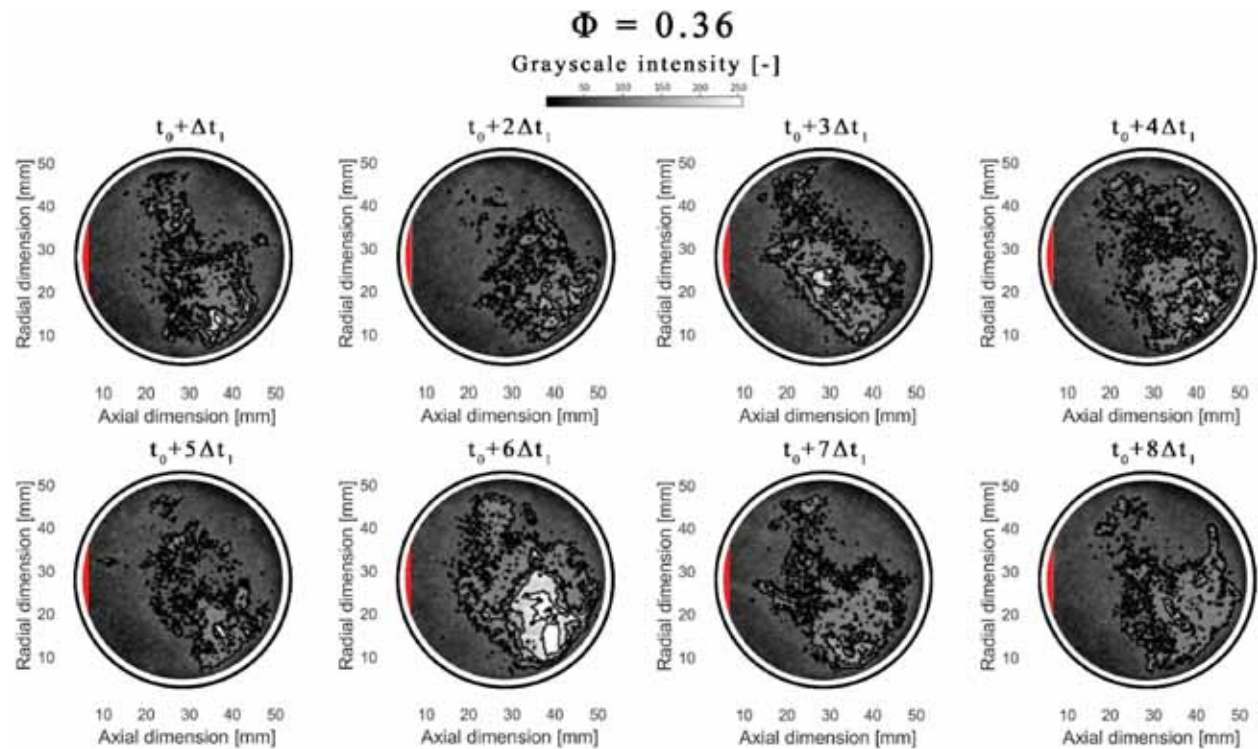

Fig. 7. Visualization through circular quartz window of the instantaneous flame dynamics at various temporal instants for $\Phi = 0.36$; in red the position of the nozzle; $t_0 \sim 0.1$ s; $\Delta t_1 \sim 0.1$ s. (For interpretation of the references to color in this figure legend, the reader is referred to the Web version of this article.)
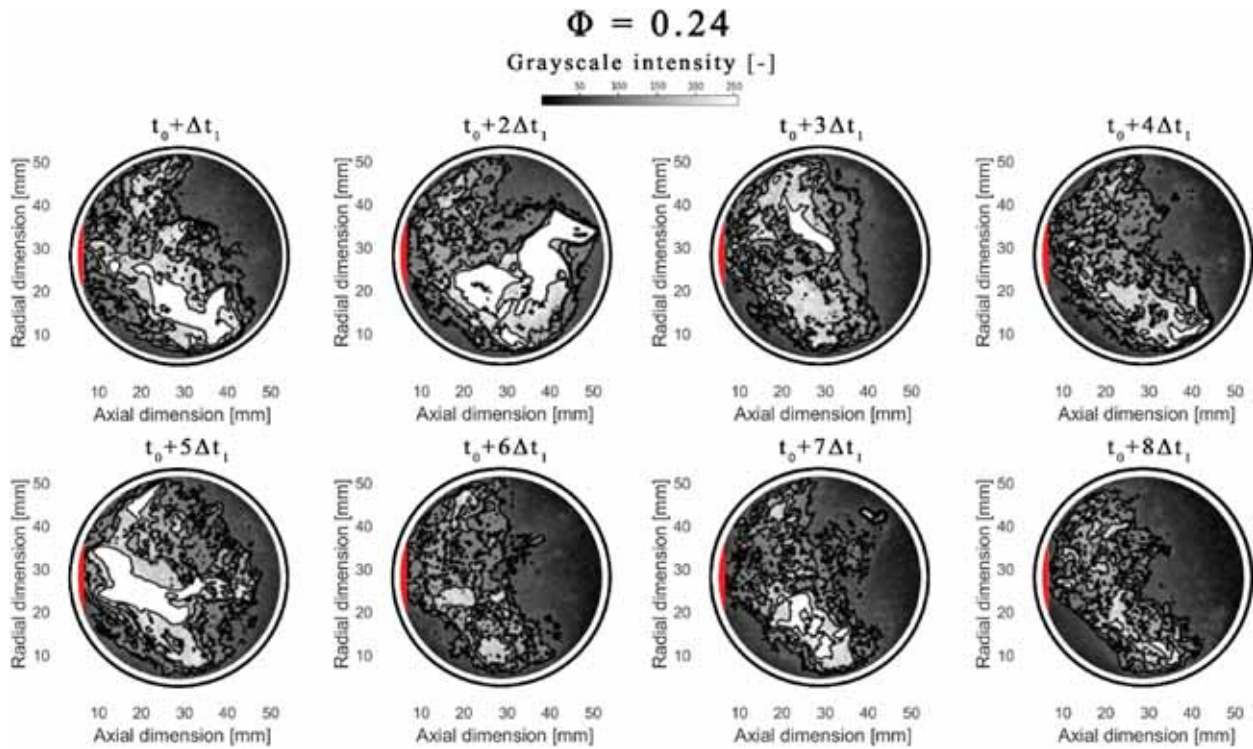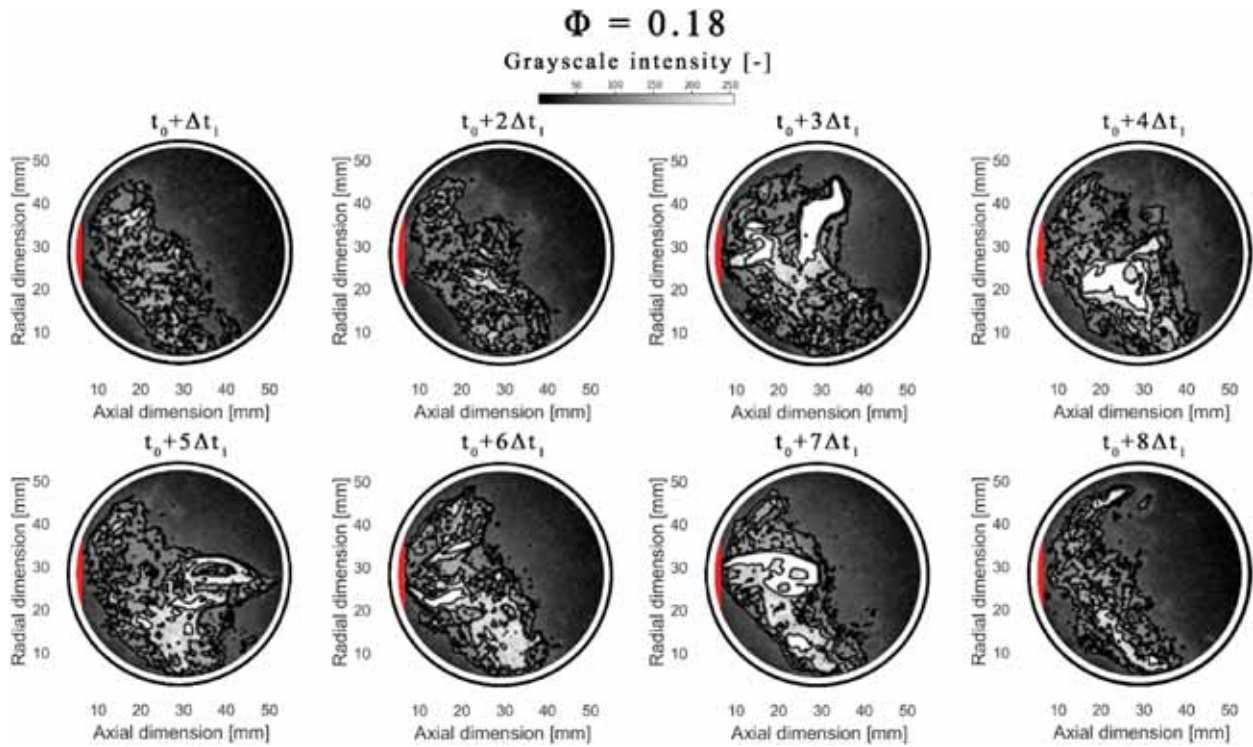
Fig. 8. Visualization through circular quartz window of the instantaneous flame dynamics at various temporal instants for $\Phi = 0.24$; in red the position of the injector nozzle; $t_0 \sim 0.1$ s; $\Delta t_1 \sim 0.1$ s. (For interpretation of the references to color in this figure legend, the reader is referred to the Web version of this article.)
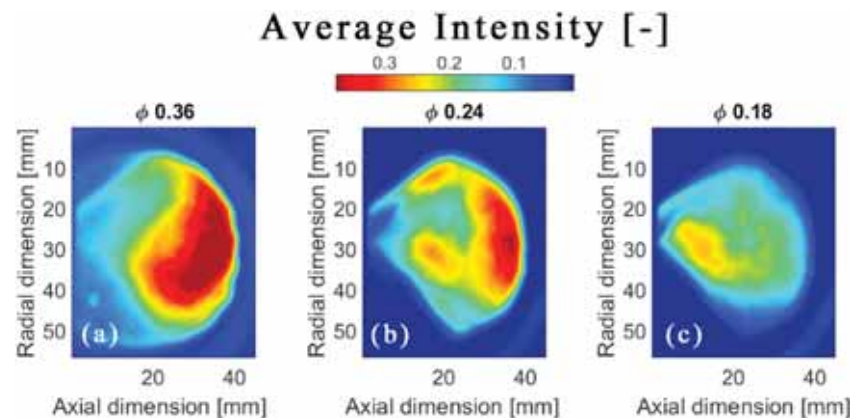

Fig. 9. Visualization through circular quartz window of the instantaneous flame dynamics at various temporal instants for $\Phi = 0.18$; in red the position of the injector nozzle; $t_0 \sim 0.1$ s; $\Delta t_1 \sim 0.1$ s. (For interpretation of the references to color in this figure legend, the reader is referred to the Web version of this article.)

Fig. 10. Average of the broadband images for Jet-A1 at different Φ acquired through the high-speed MemreCAM camera.

For the swirled spray flame, the reaction zones are primarily present in regions that are located closer to the inner shear layer between the high-velocity inflow and the inner recirculation region. In other words, the regions where the incoming air or gas flow mixes with the fuel spray and creates a swirling motion are where the reaction zones are located. These zones are characterized by prominent levels of turbulence, mixing, and combustion, which lead to the production of heat, light, and other combustion products. Therefore, the inner shear layer between the high-velocity inflow and the inner recirculation region is a critical region for understanding the combustion dynamics of swirl spray flames.

As the global equivalence ratio (Φ) decreases, the flame shifts toward the burner, suggesting a tendency for propagation along fuel mole fractions that are closer to the stoichiometric value. For $\Phi = 0.36$ the flame showed the development of combustion away from the injector area and was rather evenly distributed within a significant portion of the combustor and a relatively small intensity (see Fig. 11(a)). As Φ decreases (as shown in Fig. 11(b) and (c)), the heat release zone of the flame undergoes a contraction, forming a compact and highly localized "doughnut" ring. Simultaneously, the average flame progresses closer to the spray zone. The spatial increase in luminance variance is evident through the expansion of the red region, as observed in the comparison between Fig. 11(d), (e), and (f). The difference in the chemiluminescence intensity can be due to faster evaporation. Increased airflow rates facilitate the generation of finer sprays, improve droplet evaporation, and promote vapor-air mixing by generating stronger turbulence. This results in an improvement in the premixed nature of the spray combustion process, making it more efficient.

By coupling the average image (Fig. 11(c)) and the luminance variance (Fig. 11(f)) a more unstable flame behavior for $\Phi = 0.18$ is present, characterized by a regime near LBO conditions, with greater variance value at the flame root near the injector. The rise in the variance of OH* emissions is due to the increase of the flame fluctuations, as emphasized by the results obtained from the spectral analysis of the pressure signals.

3.3. Combustion structure of Jet-A1 fuel: POD analysis

Contemporary gas turbines often employ intense turbulent swirling patterns to stabilize flames via vortex breakdown, which creates a central recirculation zone (CRZ) along with associated shear layers. In restricted flows, like those encountered in combustion chambers of gas turbines, inner shear layers (ISL) and outer shear layers (OSL) occur between the jet and the central recirculation zone, and between the jet and the outer recirculation zone (ORZ), respectively. These shear layers are susceptible to hydrodynamic instabilities, such as the PVC - a global self-excited instability with azimuthal wavenumber - and a convective Kelvin–Helmholtz (KH) type instability. Normally, attached V-flames exhibit a dampened PVC instability because of the stabilizing influence of the density field at the combustor inlet [48], whereas the PVC instability remains unstable in the case of detached M-flames.

The mPOD analysis on chemiluminescence images is an effective tool in capturing the underlying structures associated with these instabilities in a swirled liquid-fueled combustor. Swirled flames are often characterized by a broad range of length and time scales, which can make it difficult to accurately capture the underlying flow dynamics using traditional techniques such as classical POD or DMD. By contrast, mPOD can effectively identify and separate the different length and time scales that are important in the system, providing a more accurate and comprehensive understanding of the flow dynamics. Furthermore, mPOD can also capture the interactions between different scales in the system, which is particularly valuable in the study of complex, swirling flows.

In the following subsection, the modal decomposition technique POD (Proper Orthogonal Decomposition) is performed, allowing to select the temporal filters to be applied for the mPOD technique. The entire post-processing phase has been studied using user-defined routines customized with MATLAB software.

POD analysis was conducted on high-speed chemiluminescence visualizations in a previous study [19] to examine the flame dynamics and assess its stability. The application of POD has also been extended to OH* chemiluminescence emissions. The first eight main modes which are the most energetic ones, and they describe the spatial dynamics of the flame. The cumulative distribution, in Fig. 12, for each test case is crucial for evaluating how much of the overall energy of the system is captured by a certain number of POD modes. The energy distribution of POD modes reflects their relative importance in image reconstruction. The more elevated the modal energy, the more significant its role becomes in the dynamics of the flame. Fig. 12 highlights the establishment of a more unstable
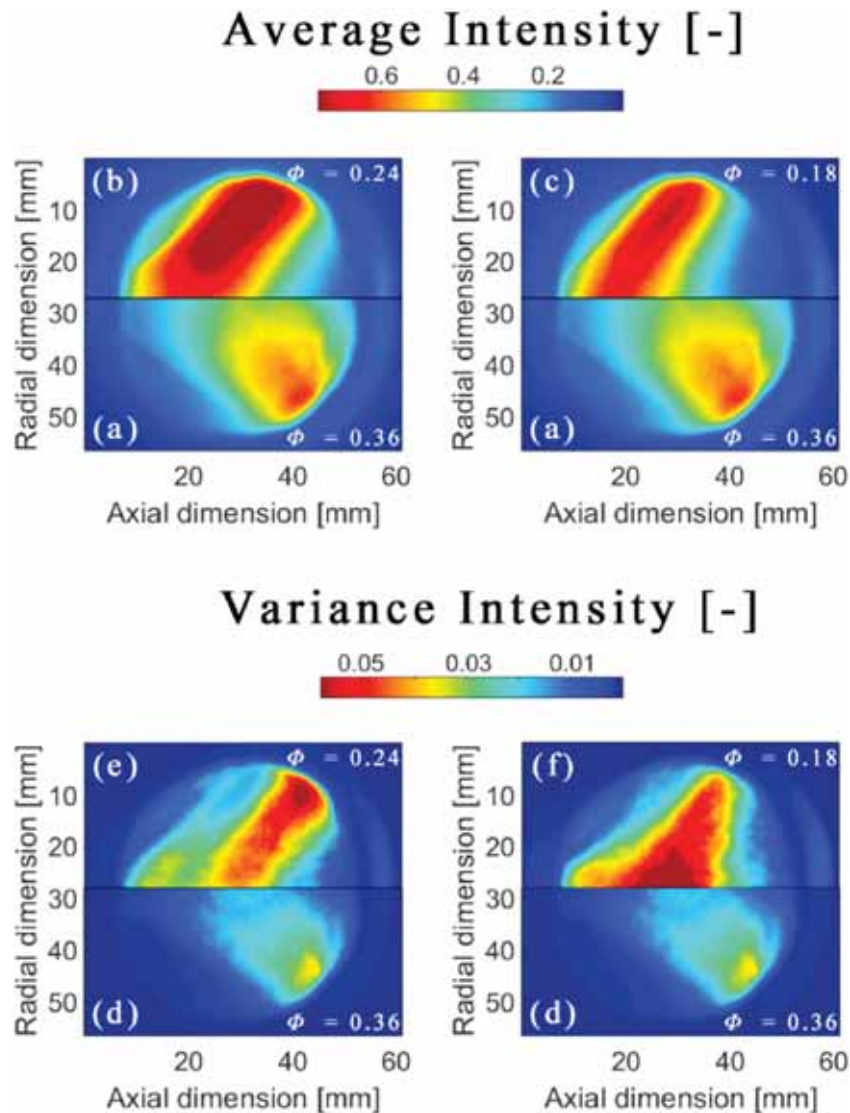
Fig. 11. Average and variance images of OH*chemiluminescence emissions for Jet-A1 at different Φ acquired through the high-speed camera ICCD equipped with OH* filter (To understand the meaning of the color references in this Figure legend, please consult the online version of this article for interpretation). (For interpretation of the references to color in this figure legend, the reader is referred to the Web version of this article.)

flame regime when reducing the global equivalence ratio from $\Phi = 0.36$ (black) to $\Phi = 0.18$ (blue), as retrieved and described in Ref. [19].

The first mode, which represents the variance related to the main flame fluctuations, has a much higher energy content than the others, even if these high order modes have a lower energy content, they could be significant to describe the presence of instability in the flame. The energy in mode 1 increases of about 20% from $\Phi = 0.36$ to $\Phi = 0.18$. This rise of energy contribution between the two fueling conditions agrees with the increase of the RMS$_{wd}$ of the acquired pressure (Fig. 6(b)), which increases of more than 20% in the bands with frequencies higher than 19.5 Hz. This confirms the evidence of increased oscillations for the leanest fueling condition, close to LBO. Then starting from mode 2, the difference between the energy contents in the different cases became marginal for POD modes. Figs. 13–15 show the POD eigenstructures retrieved for all test cases, respectively. The red or blue hue indicates the direction of pulsation, with intensity reflecting the strength of the pulsation. These pulsation regions correspond to the oscillations of the flame. It is worth observing that the most energetically weak modes (for example from mode 4 to mode 8 of all test cases, Fig. 12) own a large number of small structures, which is symptom of any instability (Fig. 13(d)–(h), Fig. 14(d)–(h) and Fig. 15(d)-(h)).

The initial three modes predominantly exhibit longitudinal oscillation, followed by subsequent modes incorporating swirling flame motion, and the higher modes capturing turbulent flame motion characterized by low perturbation intensity and a minimal energy fraction. Furthermore, if Φ decreases the flame becomes more unstable, the eigenstructure of 1st POD mode moves toward the spray injector. At very lean conditions, the flame stabilizes in regions of high fluid dynamic strain rate closer to the burner exit. This aligns
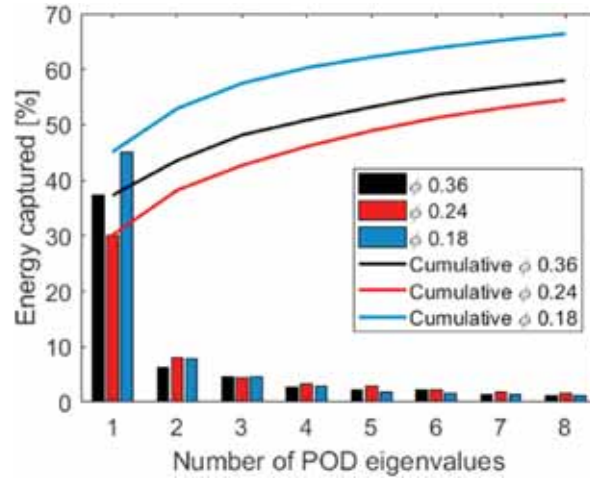
Fig. 12. Comparison of the three test cases of the energy of each POD eigenvalue through both relative and cumulative distribution.
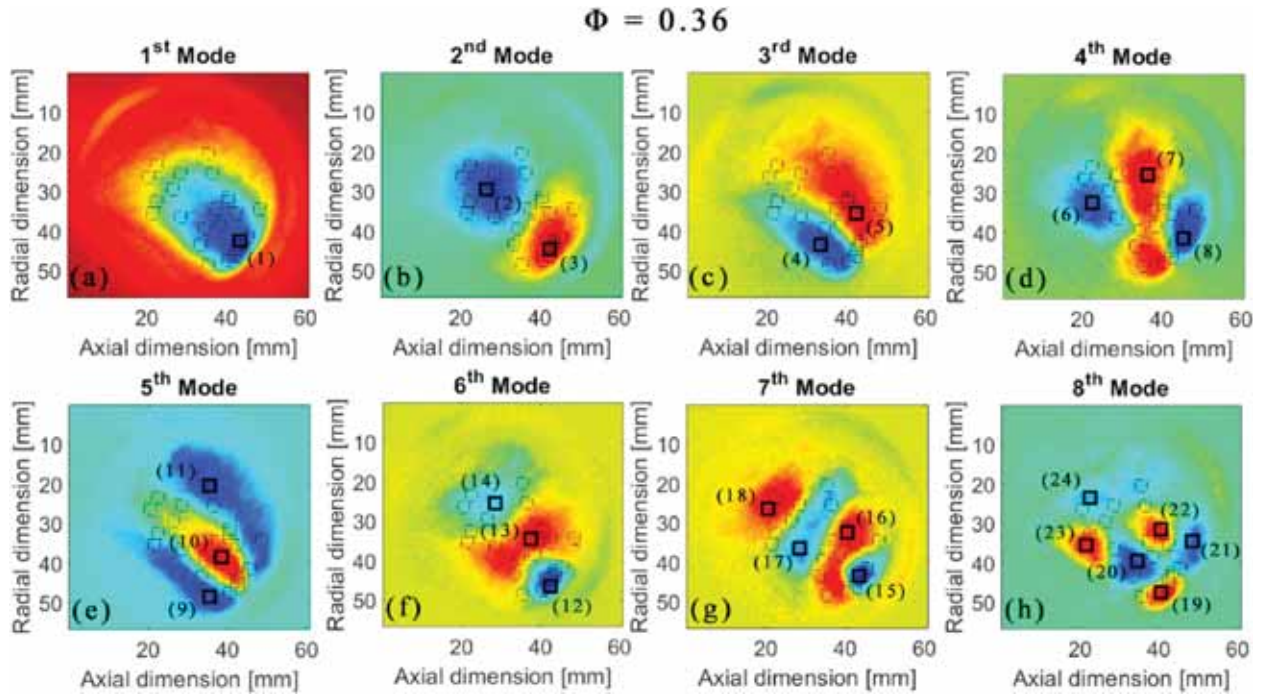

Fig. 13. POD modes 1–8 for OH* chemiluminescence emission for $\Phi = 0.36$. The squares correspond to specific regions of interest in the flame, ROI of Table 2. Color meanings detailed online. (For interpretation of the references to color in this figure legend, the reader is referred to the Web version of this article.)

with findings in Ref. [49], which elucidated the progressive upstream stabilization of the flame with decreasing Φ through a flow-flame balance.

A swirl spray flame typically exhibits elevated levels of velocity fluctuations, causing the flame to oscillate back and forth axially between two distinct combustion regimes. The first regime corresponds to an inner flame that is anchored to the fuel spray, located a few millimeters from the injection system's exit. This regime is evident from the mode 1 of flame at $\Phi = 0.24$ and 0.18 (Figs. 14 and 15). The second regime is characterized by a lifted flame, which is situated far from the fuel spray's top, spreading the flame over large horizontal distances, as evident for the mode 1 of flame at $\Phi = 0.36$ (Fig. 13). Between these two combustion regimes, the base of the inner flame oscillates, moving between the two extreme positions. In our experiments mode 1 for $\Phi = 0.24$ and 0.18 shows that as LBO approaches, the angle of the swirling shear layer decreases, resulting in reduced radial outward movement of droplets and greater confinement around the PVC. Furthermore, this mode exhibit roughly opposite distribution for the two different fuel/air ratio, suggesting a phase-delay behavior of the oscillating flames for these two fueling conditions.

On the other hand, the eigenstructures of 2nd and 3rd POD modes are quite similar. At $\Phi = 0.36$, mode 4 shows axial oscillations
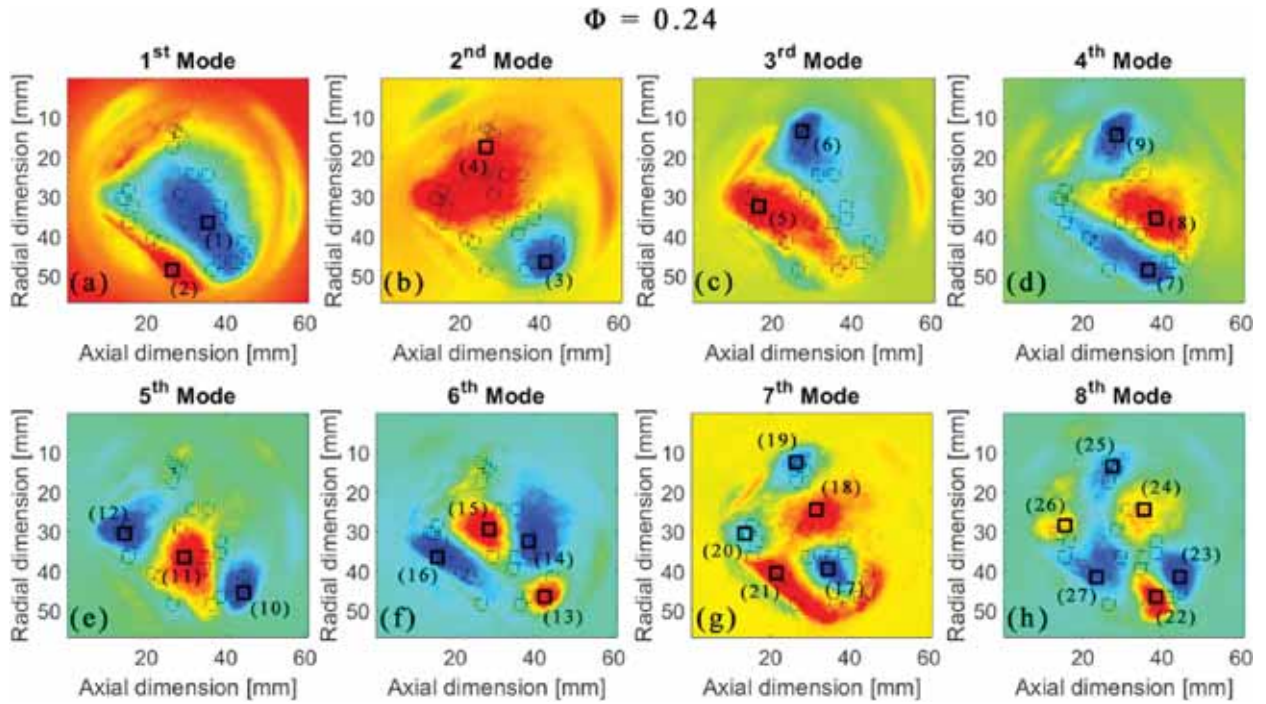
Fig. 14. POD modes 1–8 for OH* chemiluminescence emission for $\Phi = 0.24$. The squares correspond to specific regions of interest in the flame, ROI of Table 2. Color meanings detailed online. (For interpretation of the references to color in this figure legend, the reader is referred to the Web version of this article.)
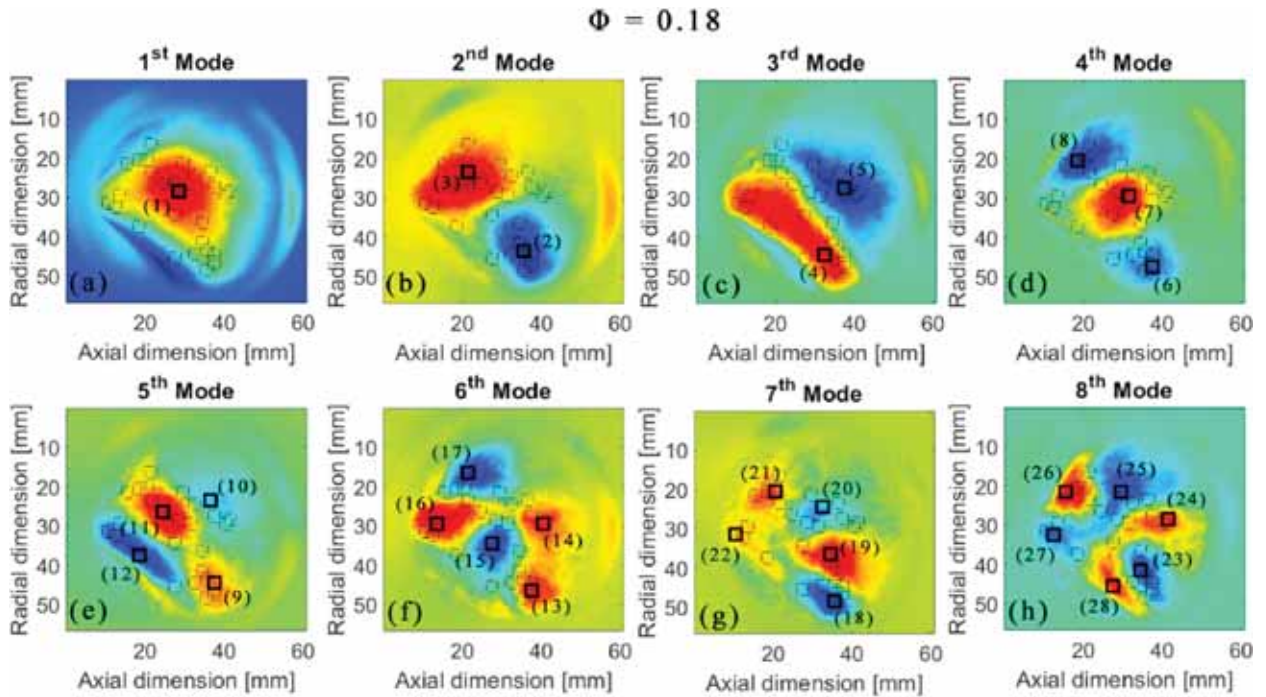

Fig. 15. POD modes 1–8 for OH* chemiluminescence emission for $\Phi = 0.18$. The squares correspond to specific regions of interest in the flame, ROI of Table 2. Color meanings detailed online. (For interpretation of the references to color in this figure legend, the reader is referred to the Web version of this article.)

with structures while lowering Φ fluctuations in the outer zones of the flame are evident that are out-of-phase with fluctuations in the center. Furthermore, mode 5 presents more structures at the leanest condition ($\Phi = 0.18$).

In addition to the spatial distribution and energy contribution of each mode, the wavelet decomposition of the energy λ_i was

calculated. The λ_i values are scalar quantities representing the amount of energy captured by each mode from the overall dataset. The higher the value of λ, the more significant that mode is in terms of capturing the dynamics or structure of the dataset. The application of wavelet decomposition in this context refers to the time-dependent coefficients associated with each POD mode. Fig. 16 then shows the decomposition of the energy contents in the ranges A0: [0–31.25] Hz, A1: [31.25–62.5] Hz, A2: [62.25–125] Hz, A3: [125–250] Hz, A4: [250–500] Hz, associated with each mode. The A0 range for all three test cases (Fig. 16(a)–(c)) and for all modes is predominant over the others, indicating how the energy content in the [0–31.25] Hz range is the most important. Test case $\Phi = 0.18$ (Fig. 16(c)), in general, shows lower maximum values than the other two test cases; this is because the total energy was distributed toward less significant modes that represent more instability. The energy content of test case $\Phi = 0.24$ exhibits some values higher than those of test case $\Phi = 0.36$ and some lower; this energy behavior is because the flame, under these combustion conditions, exhibits a transition behavior between lean (test case $\Phi = 0.36$) and ultra-lean (test case $\Phi = 0.24$) combustion.

Additionally, an examination of its evolution in the frequency domain has been carried out utilizing the information present in the time coefficients. The Fast Fourier Transform (FFT) was employed to discern the frequency of the most significant coherent structures represented by the POD modes.

Fig. 17 shows the temporal coefficient evolution and the frequency analysis of the 4 modes determined by Fast Fourier Transform (FFT) for the test cases $\Phi = 0.36$, $\Phi = 0.24$ and $\Phi = 0.18$. The temporal coefficient evolution and the FFTs of the remaining modes of higher order than mode 5 appears almost flat and therefore not shown in the figures.

From $\Phi = 0.36$ to $\Phi = 0.18$, the oscillations in the temporal coefficient evolution amplify as the value of Φ decreases, becoming more significant in higher modes as well. These oscillations increase due to the growing flame instability. This, in turn, is also reflected in the frequency behavior. The energy strength of each spatial mode becomes apparent in the FFTs of the time coefficients related to their respective modes. The consistently high energy content observed in modes 1 and 2 is confirmed for all the cases, while the spectral content of the mode 3 and 4 appears nearly flat at $\Phi = 0.36$ and shows some peaks for the leanest condition, $\Phi = 0.18$. The first mode presents some relevant peaks for frequency below 50 Hz, with the highest amplitude at $\Phi = 0.18$. At $\Phi = 0.36$ the FFTs of POD modes higher than 1 didn't show dominant frequencies and high FFT amplitude or peaks, while lowering Φ, the second and third modes show a rise in the FFT amplitude for the low-frequency range, lower than 50 Hz.

Based on the spatial analysis of the POD eigenstructures, specific flame region of interest (ROI) have been identified (see the black squares in Figs. 13–15) and categorized through increasing numbers from (1) to (24) for test case $\Phi = 0.36$, from (1) to (27) for test case $\Phi = 0.24$ and from (1) to (28) for test case $\Phi = 0.18$ (see Table 2). The ROIs were identified by taking the absolute highest intensity pixels of each structure. In all these ROIs, the FFT of the temporal series of POD mode has been applied to highlight the characteristic frequencies of each modal structure for each test case. Table 2 reports the two most relevant frequencies, which have been used to select the frequency band-pass filters used in DMD and mPOD computations: 3–9 Hz, 10–14 Hz, 15–19 Hz and 24–30 Hz.

3.4. Combustion structure of Jet-A1 fuel: DMD analysis

In this section, the Dynamic Mode Decomposition (DMD) technique has been implemented on the same flame image dataset and the imaging analysis of the DMD modal structures has been based on the most relevant frequencies previously detected and reported in Tables 2, i.e.

- $\Phi = 0.36$: 4.21 Hz, 5.19 Hz, 9.69 Hz, 17.22 Hz, and 27.18 Hz;
- $\Phi = 0.24$: 1.06 Hz, 1.96 Hz, 4.07 Hz, 8.96 Hz, 9.18 Hz, 17.98 Hz, and 24.65 Hz;
- $\Phi = 0.18$: 3.17 Hz, 5.26 Hz, 6.44 Hz, 7.44 Hz, 12.10 Hz, 13.40 Hz, and 29.26 Hz.

DMD, unlike POD, can associate each spatial structure with its respective frequency. Figs. 18–20 show the corresponding modal
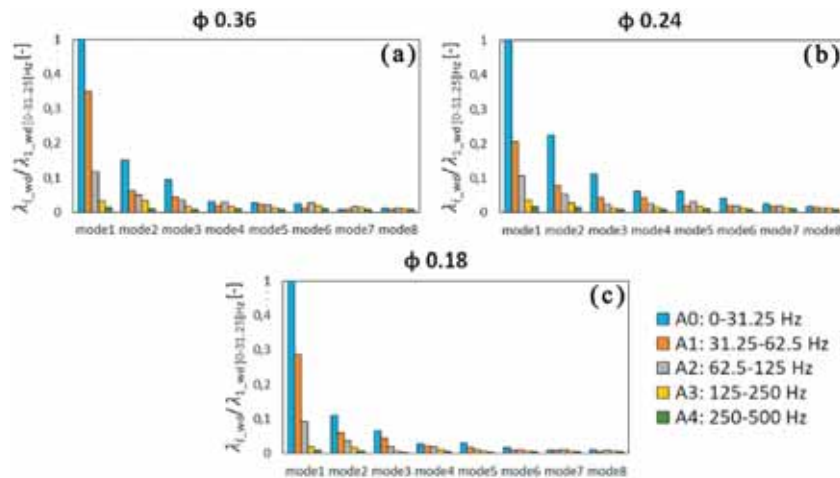

Fig. 16. Wavelet of the energy λ_i extracted from the POD of each mode dimensionless values with respect to the one in the range [0–31.25] Hz, of the test cases: a) $\Phi = 0.36$, b) $\Phi = 0.24$, c) $\Phi = 0.18$.
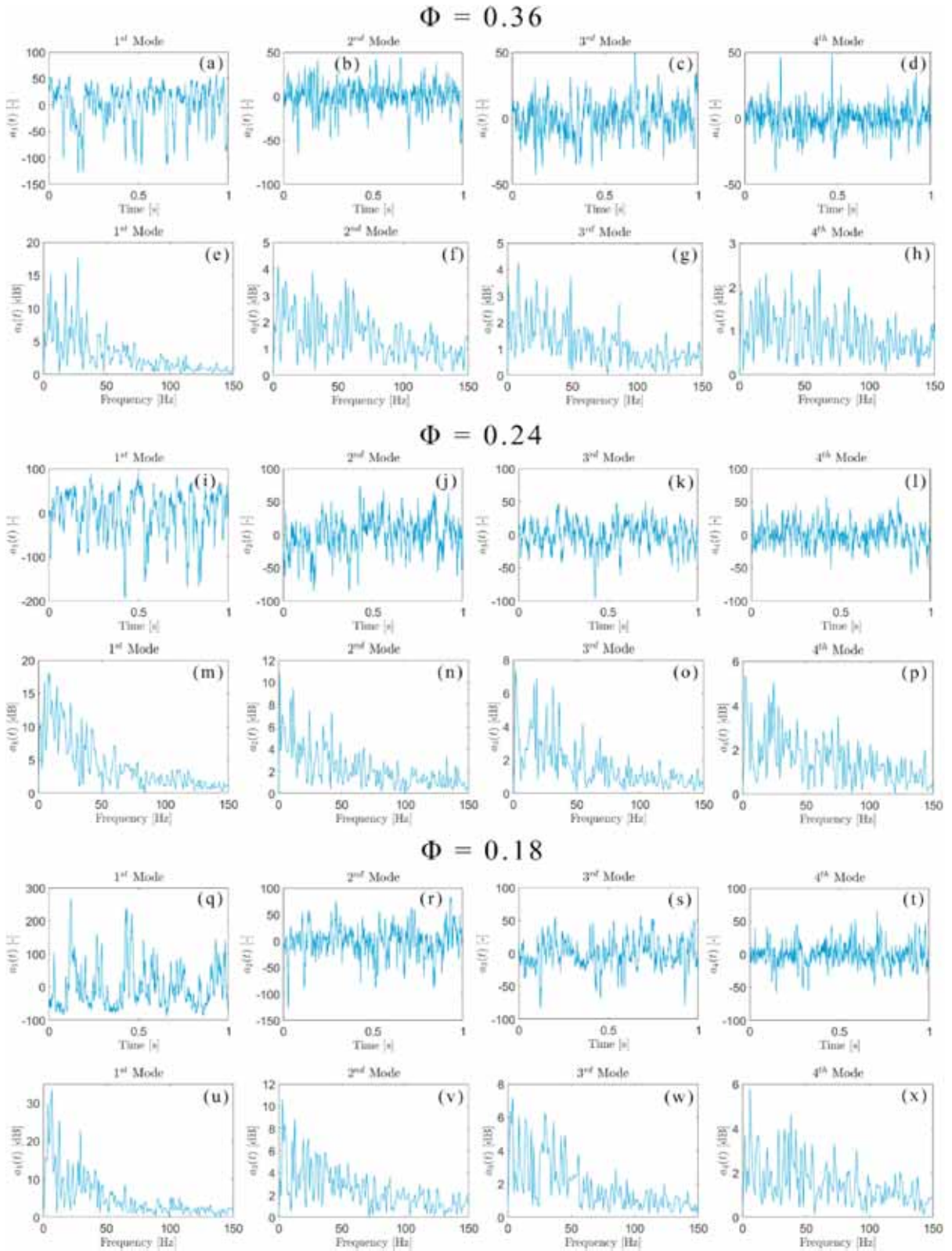
Fig. 17. Temporal coefficient evolution (a)–(d), (i)–(l), (q)–(t) and FFTs (e)–(h), (m)–(p), (u)–(x) of the first 4 eigenvalues of the POD for OH* chemiluminescence emission for $\Phi = 0.36$, $\Phi = 0.24$ and $\Phi = 0.18$.

Table 2
Frequencies (F1 and F2) relative to the first two maximum amplitude of the investigated areas of Figs. 13–15 through the FFT.

$\Phi = 0.36$				$\Phi = 0.24$				$\Phi = 0.18$			
Mode	ROI	F1 [Hz]	F2 [Hz]	Mode	ROI	F1 [Hz]	F2 [Hz]	Mode	ROI	F1 [Hz]	F2 [Hz]
1	(1)	27.34	5.86	1	(1)	4.88	7.81	1	(1)	5.86	3.91
2	(2)	9.77	27.34		(2)	0.98	26.37	2	(2)	29.30	2.93
	(3)	27.34	5.86	2	(3)	24.41	4.88		(3)	3.91	5.86
3	(4)	27.34	5.86		(4)	1.95	31.25	3	(4)	29.30	12.70
	(5)	5.86	17.58	3	(5)	0.98	18.55		(5)	5.86	12.70
4	(6)	17.58	5.86		(6)	1.95	31.25	4	(6)	29.30	2.93
	(7)	27.34	17.58	4	(7)	31.25	19.53		(7)	5.86	3.91
	(8)	5.86	27.34		(8)	7.81	4.88		(8)	5.86	12.70
					(9)	1.95	31.25				

DMD structures corresponding at the frequencies specified above. In general, it is noted that the lack of sharpness of the structures and the presence of high noise in the images does not help to define the structures of the flame dynamics. Fig. 18 corresponds to the spatial structures of the flame dynamics of the test case $\Phi = 0.36$. Fig. 18(a) and (c) are similar to the structure of Fig. 13(b) where a doublet structure is present, Fig. 18(a), (b) and (d) have a structure that is associated with Fig. 13(a). The observed peaks in the damping ratio and decay rate confirm the frequencies selected for analysis. For this test case, the greater damping occurs in the order of 6.46 Hz, and at the same frequency, the fastest decay also occurs. Fig. 19 describes the spatial structures of the flame dynamics of the test case $\Phi = 0.24$ Notably, the spatial configuration depicted in Fig. 19(a) mirrors that of Fig. 14(a), and Fig. 19(b) closely resembles Fig. 14(b), attributed to their common triplet structure. Likewise, Fig. 19(c) is reminiscent of Fig. 14(d), showcasing a similar triplet formation, while Fig. 19(d) parallels the structure shown in Fig. 14(c). The structure in Fig. 19(b) possesses the same frequency identified among the peaks of the damping ratio and decay rate, while the other spatial structures have frequencies close to those identified by the damping and decay rate. Fig. 20 corresponds to the spatial structures of the relative frequencies of the test case $\Phi = 0.18$. Fig. 20(a) and (c) represent the extraction of a doublet structure that is associated with Fig. 15(b)–. 20(d) has a structure that describes the same flame dynamics and are similar to Fig. 15(a). Finally, Fig. 20(d) has unclear structures and are associated with Fig. 15(g) and (h), respectively. For this test case, the frequency peaks identified in both the damping and decay rate plots closely align with the frequencies of the spatial structures, affirming the accurate selection of characteristic frequencies.

3.5. Combustion structure of Jet-A1 fuel: mPOD analysis

The primary advantage of DMD and mPOD lies in the organization of modes based on dominant frequencies. This contrasts with POD, where multiple frequencies are amalgamated, rendering it more challenging to comprehend the distinct influence of a singular frequency. POD analysis can explore the primary pulsation region, but each mode exhibits a complex multiple-frequency spectrum, making it challenging to discern the associated flow structure at each frequency. Applying mPOD could offer a fresh perspective in uncovering instability details. The benefit of mPOD analysis lies in its ability to correlate the flame structure with the characteristics of the frequency spectrum.

Hence the following subsection describes the results obtained from the use of mPOD to the OH* chemiluminescence emissions. The mPOD integrates multi-resolution analysis through filter banks and standard POD to generate modes that are optimal within a specific range of frequencies (scales). In this work, therefore, a strategy was introduced to determine the filtering frequencies to be applied to the mPOD, described in the previous section 3.2. As shown in previous section, the flames of $\Phi = 0.36$ corresponds to lean stable conditions, and the flames of $\Phi = 0.24$ and $\Phi = 0.18$ represents near-LBO conditions. Within a spray-swirled combustor, the newly formed mixture of droplets, vapor, and air exiting the injector is transported downstream across the swirling shear layer. Simultaneously, the hot product, unreacted vapor, and unevaporated droplets recirculate upstream toward the forward stagnant point of the vortex breakdown, where they blend with the fresh fuel-air mixture [50]. When a high swirl number is present, the tangential velocity component generates an internal recirculation zone (IRZ) around the centerline of the combustor, leading to the phenomenon of vortex breakdown. This breakdown is typically accompanied by the formation of large-scale coherent structures [51].

Fig. 21 shows the mPOD spatial structures and the FFT of the mPOD temporal eigenfunctions, while Fig. 22 shows the temporal behavior of the eigenvalues for the stable flame condition ($\Phi = 0.36$). Modes 1–3 correspond to the same coherent structure as POD mode 1, shown in Fig. 13(a). The FFT analysis in Fig. 21(e)–(h) shows that the dominant frequencies for these modes align with the dominant and sub-dominant frequencies identified in the POD analysis, shown in Fig. 17. The mPOD mode 2 (Fig. 22(b)) shows a clear burst phenomenon characterized by axial oscillations that are a succession of sinusoids with varying amplitudes. Low-amplitude bursts precede high-amplitude bursts. This is confirmed by the FFT in Fig. 21(f), which shows a frequency of 27.18 Hz. Mode 3 of mPOD (Fig. 22(c)) also shows a hint of the burst phenomenon, although less prominent and with smaller amplitudes compared to mode 2. The high frequencies (i.e., around 21 and 27 Hz) are related to the main inner flame structure, similar to that in POD mode 1 (Fig. 13(a)). In the transition between stable and quasi-LBO conditions ($\Phi = 0.24$), the modes 1, 2 and 3 in Fig. 23(a), (b), and (c) show coherent structures of axially centered OH* emission. These modes are similar to the first POD mode in Fig. 17(m), but without frequency overlap. In these three mPOD modes it is possible to identify a large flame structure in the inner region, near the nozzle, along with two smaller structures in the outer recirculation zone, structures due to the fuel spray forming a V-shape. Generally, the evolution of these structures depends on atomization, vaporization, and mixing, along with the dynamics of the flame front; thus, the variation of Φ has a significant impact on their development. Although they have structures similar to the first POD mode, after filtering, the three mPOD
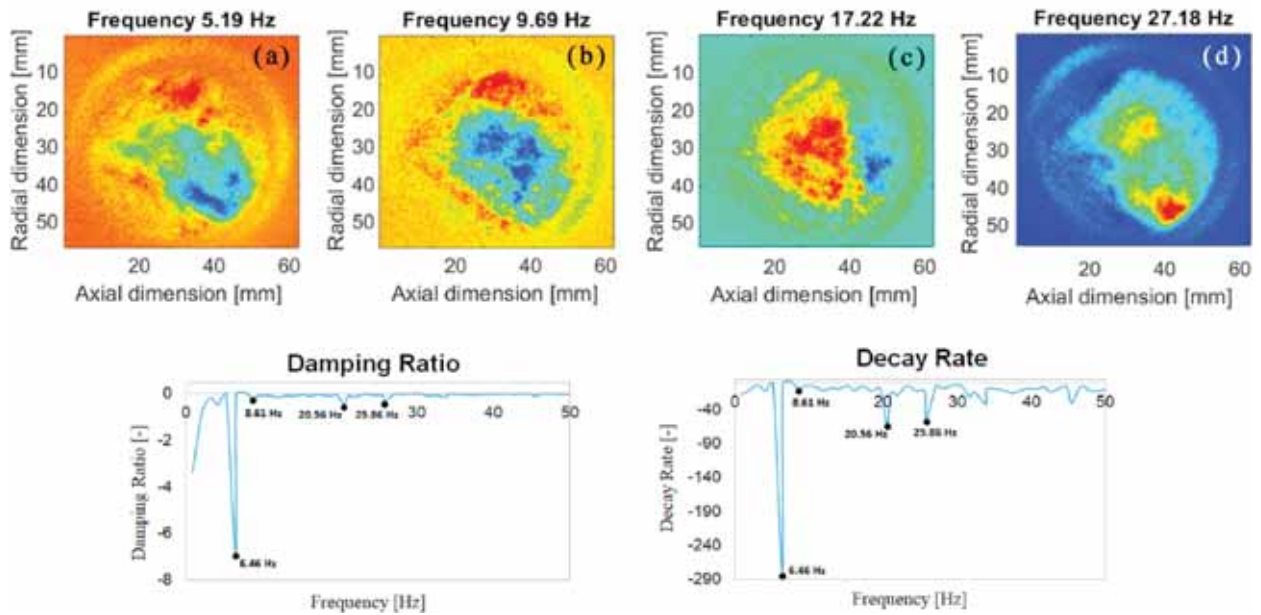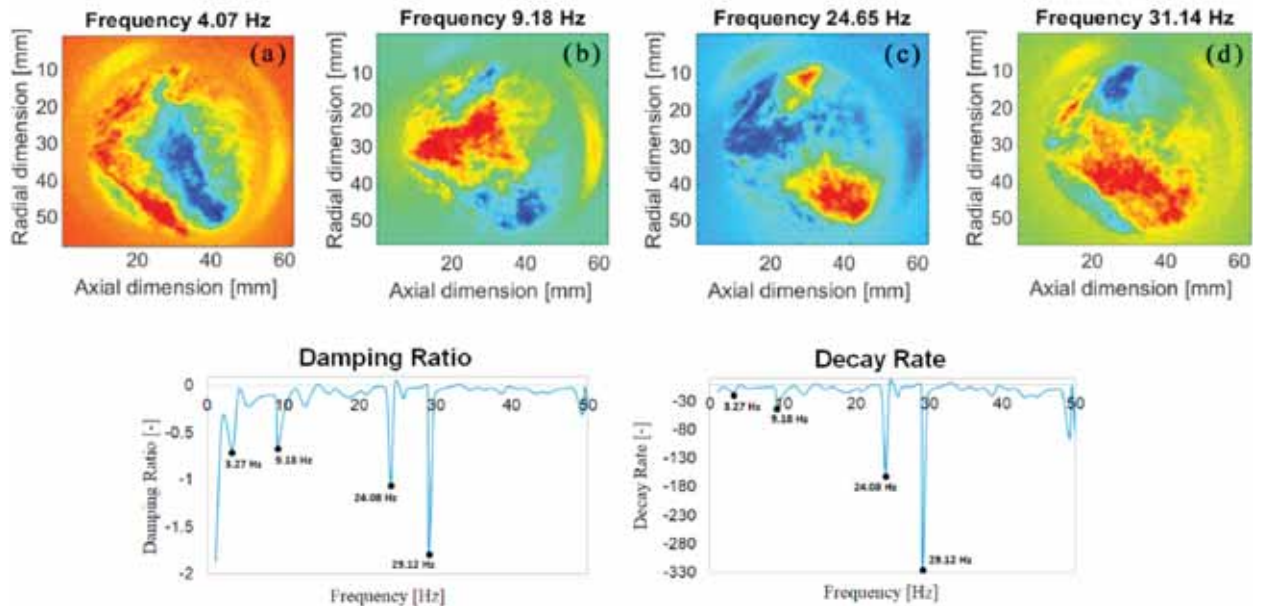
Fig. 18. Dynamic flame structures from OH* chemiluminescence at frequencies in Table 2 ($\Phi = 0.36$) shown above; below are their damping ratios and decay rates. Color meanings detailed online. (For interpretation of the references to color in this figure legend, the reader is referred to the Web version of this article.)

Fig. 19. Dynamic flame structures from OH* chemiluminescence at frequencies in Table 2 ($\Phi = 0.24$) shown above; below are their damping ratios and decay rates. Color meanings detailed online. (For interpretation of the references to color in this figure legend, the reader is referred to the Web version of this article.)

modes have different frequencies ranging from 6.49 to 20.21 Hz. The mode 2 (Fig. 23(b)) exhibits burst behavior with irregular large-amplitude periodic oscillations. The mode 3 (Fig. 23(c)) shows burst phenomena similar to those seen in mode 2, characterized by irregular amplitudes. The fourth mPOD mode (Fig. 23(d)) is like the self-structure of POD mode 4 (Fig. 14(d)). The temporal progression of its eigenvalues (depicted in Fig. 24(d)) reveals intermittency marked by a dynamic pattern involving irregular instances of
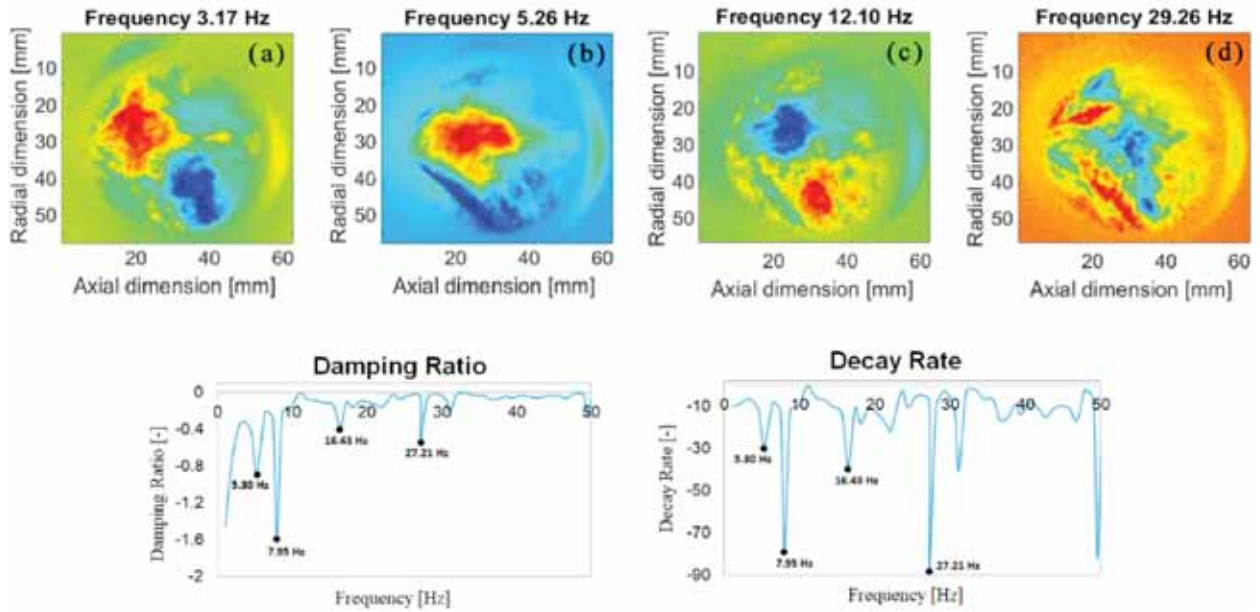
Fig. 20. Dynamic flame structures from OH* chemiluminescence at frequencies in Table 2 (Φ = 0.18) shown above; below are their damping ratios and decay rates. Color meanings detailed online. (For interpretation of the references to color in this figure legend, the reader is referred to the Web version of this article.)
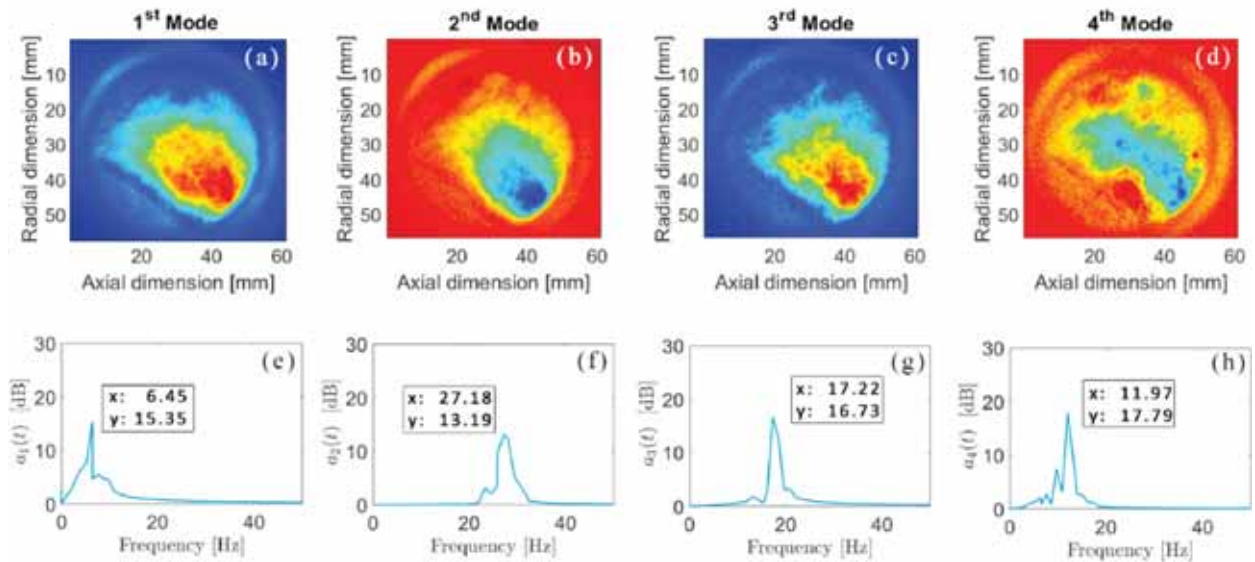

Fig. 21. mPOD Modes 1–4 of OH* Chemiluminescence for Φ = 0.36: Spatial Structures (a)–(d) and Fourier Transforms (i)–(l).

large-amplitude periodic oscillations interspersed with periods of low-amplitude aperiodic fluctuations. These axial fluctuations and an amplitude oscillation have a frequency of 26.23 Hz, as shown in Fig. 23(h). The burst phenomenon is also present in modes 3 and 7, Fig. 24(c) and (g) respectively. Mode 3 has a burst that starts from an average amplitude equal to 0 (extinction phenomenon) followed by a re-ignition with amplitudes varying over time at a frequency of 20.21 Hz. Mode 7, on the other hand, exhibits a burst phenomenon with relatively less pronounced amplitudes and at a lower frequency compared to mode 3.

As the global equivalence ratio Φ decreases to 0.18, approaching LBO conditions, the flame position shifts closer to the injector exit

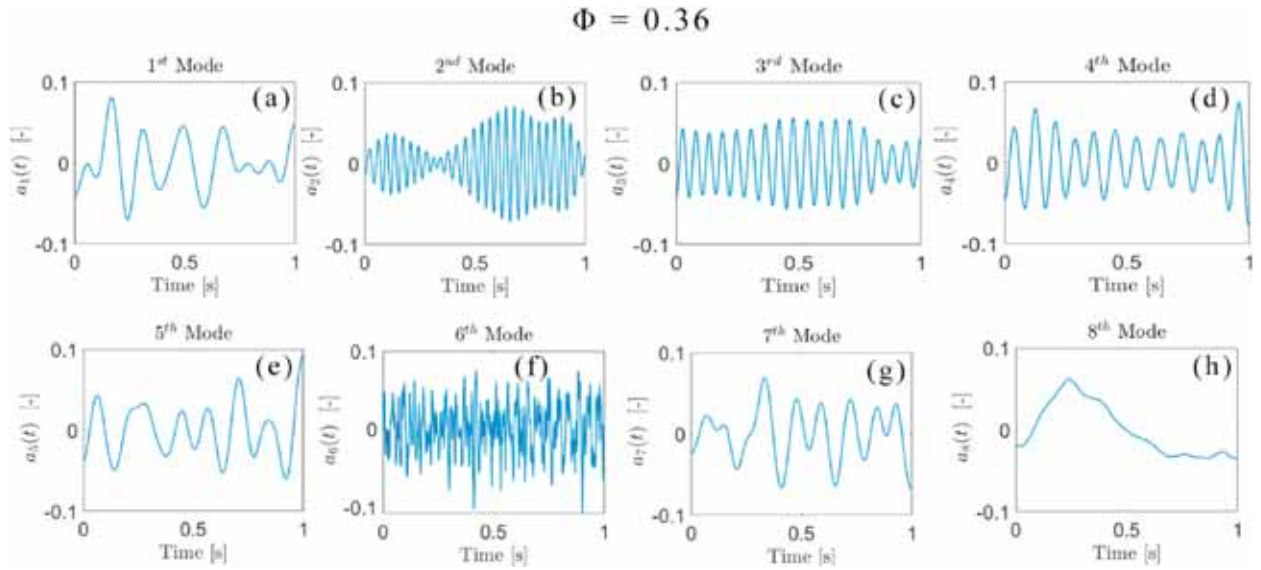**Fig. 22.** mPOD Modes 1–4 of OH* Chemiluminescence for $\Phi = 0.36$: Temporal Dynamics (a)–(h).
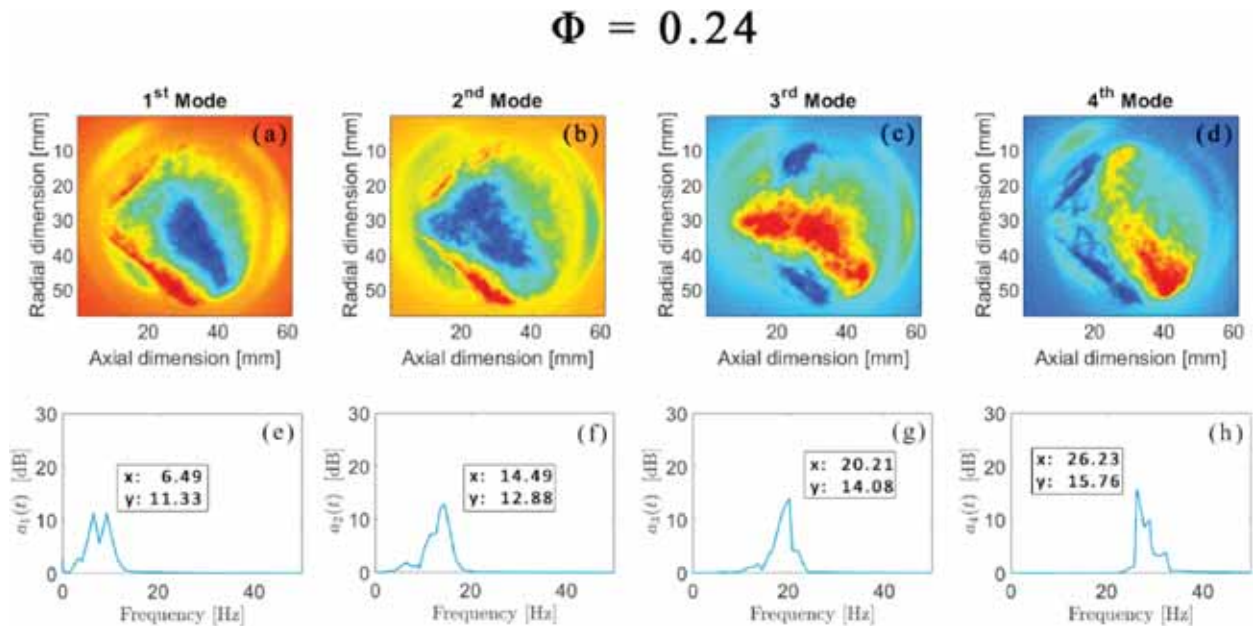

Fig. 23. mPOD Modes 1–4 of OH* Chemiluminescence for $\Phi = 0.24$: Spatial Structures (a)–(d) and Fourier Transforms (i)–(l). Color meanings detailed online. (For interpretation of the references to color in this figure legend, the reader is referred to the Web version of this article.)

(Fig. 25). The spatial structures of the mPOD modes 1 to 4 (Fig. 25(a)–(d)) are similar to POD mode 1 (Fig. 15(a)), but each mPOD mode exhibits distinct temporal and frequency dynamics. At $\Phi = 0.18$, bursts become more frequent, especially evident in mPOD modes 2, 3, 4, and 8 (Fig. 26(b), (c), (d), and (h)). The temporal behavior of mode 2 at $\Phi = 0.18$ resembles that at $\Phi = 0.36$, but with higher amplitude flame oscillations. These oscillations are characterized by a succession of flame on/offs, with bursts occurring from the injector exit towards the flame periphery, exhibiting the highest repetition frequency among all analyzed Φ values. Mode 3 (Fig. 26 (c)) shows burst phenomena with a decay motion, which is not observed at higher Φ values. Mode 4 (Fig. 26(d)) displays pronounced bursts with high-amplitude oscillations, while mode 8 (Fig. 26(h)) exhibits rapid, high-amplitude oscillations followed by periods of relative calm, indicating significant instability as the system approaches blowout conditions.

Focusing on the same mPOD mode, mode 3, across different Φ a clear transition from stable oscillations to erratic behavior as the system nears blowout is evident. At $\Phi = 0.36$, this has minor bursts with small amplitudes and scarce occurrences, indicating a stable flame condition. At $\Phi = 0.24$ bursts are more pronounced with larger amplitude oscillations and irregular intervals, showing signs of
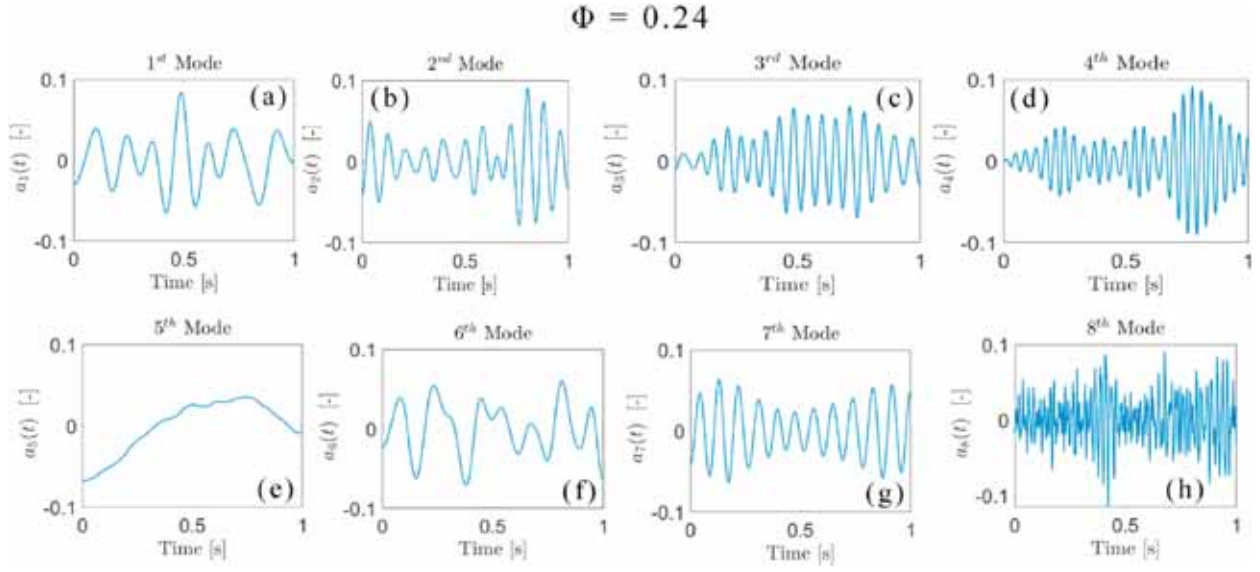
Fig. 24. mPOD Modes 1–4 of OH* Chemiluminescence for $\Phi = 0.24$: Temporal Dynamics (a)–(h).
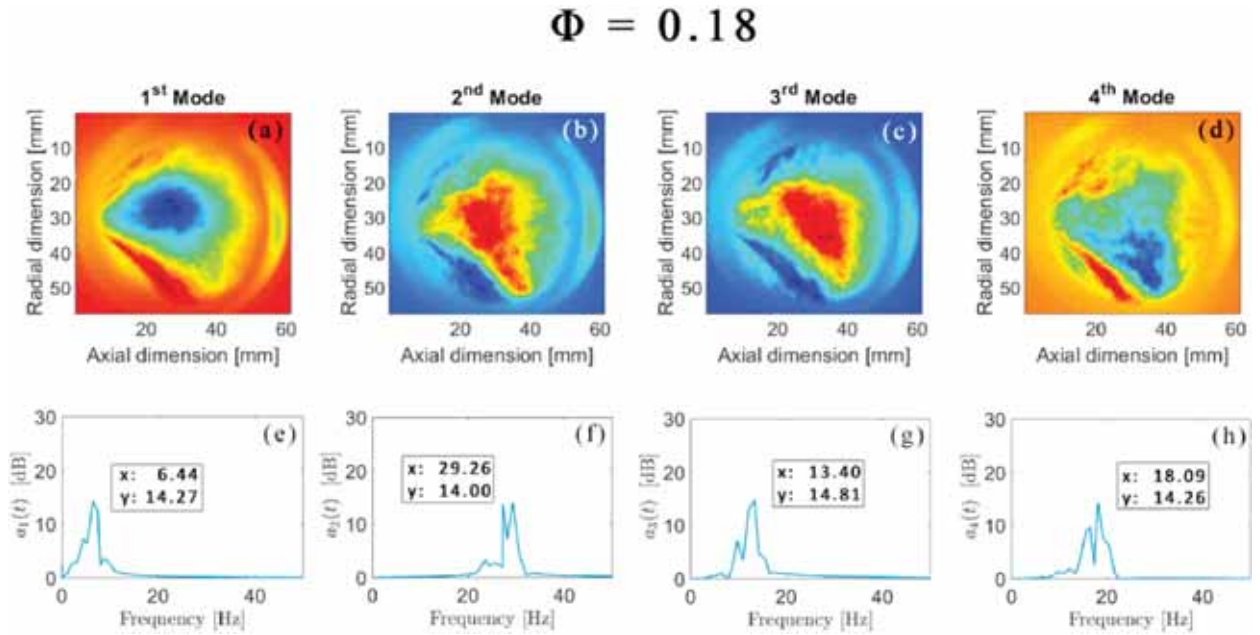

Fig. 25. mPOD Modes 1–4 of OH* Chemiluminescence for $\Phi = 0.18$: Spatial Structures (a)–(d) and Fourier Transforms (i)–(l). Color meanings detailed online. (For interpretation of the references to color in this figure legend, the reader is referred to the Web version of this article.)

intermittency and instability. At $\Phi = 0.18$ frequent high-amplitude bursts and a notable decay to nearly zero amplitude suggest potential flame extinction events followed by re-ignition, typifying the approach to lean blowout with erratic and aperiodic fluctuations.

Analysis of nonlinear mPOD eigenvalue time series has been performed to detect precursors to blowout. The autocorrelation function (ACF) is a valuable tool for understanding temporal relationships in time series data, measuring how the signal correlates with itself over various time lags. Analyzing the ACF provides insights into the periodic behavior, damping characteristics, and stability of the combustion process. Specifically, burst-like patterns in the ACF indicate intermittent dynamics, which are crucial for identifying transitions in flame behavior, especially as it approaches lean blowout conditions. The ACF is defined as:

$$R(\tau) = \frac{1}{N - \tau} \sum_{t=1}^{N-\tau} (x_t - \overline{x})(x_{t+\tau} - \overline{x}) \tag{11}$$
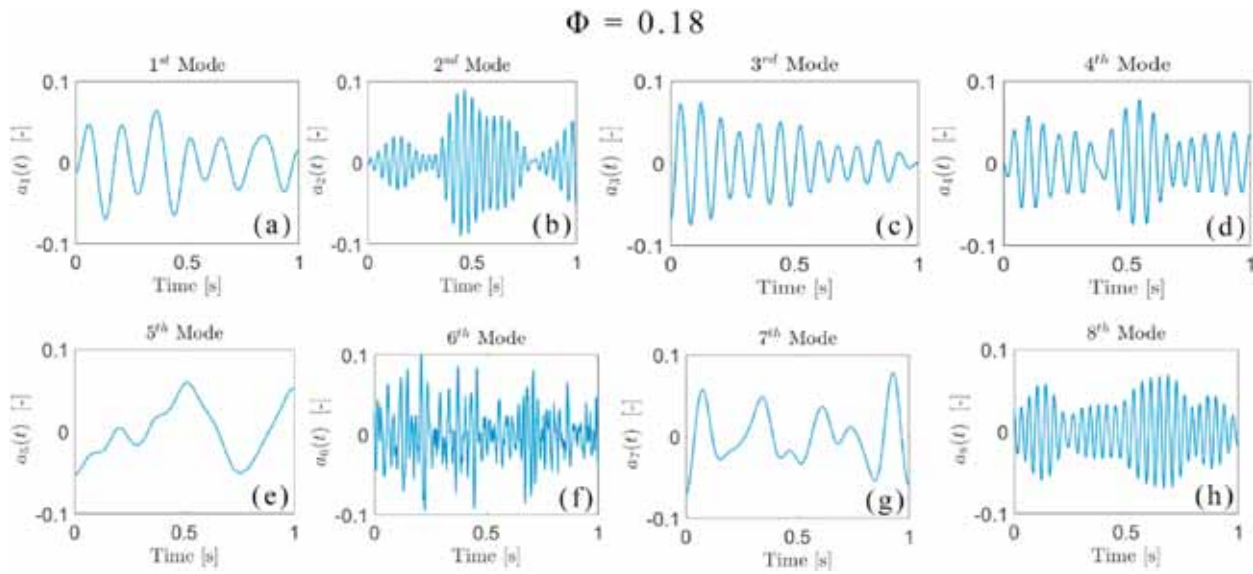
$\Phi = 0.18$

Fig. 26. mPOD Modes 1–4 of OH* Chemiluminescence for $\Phi = 0.18$: Temporal Dynamics (a)–(h).

where $R(\tau)$ is the autocorrelation at lag τ, x_t is the time series data, $\overline{x}$ is the mean of the data, and N is the number of data points. The ACF provides a measure of how the values of the time series at different times are related.

To better understand the damping characteristics and the presence of bursts, we calculate the envelope of the ACF using the Hilbert transform. In this analysis, the envelope of the autocorrelation function was calculated using the Hilbert transform [52].

Fig. 27 shows the ACF of the mPOD eigenvalues for modes 1 to 4 and their envelopes for different Φ. The ACF and its envelope help assess the stability and dynamics of the combustion system. At $\Phi = 0.36$ the ACF shows a strong initial peak followed by gradually decaying peaks. The absence of significant bursts indicates stable periodic behavior with consistent oscillations, reflecting a stable flame condition. Then at $\Phi = 0.24$ the ACF displays a strong initial peak, with subsequent peaks decaying more rapidly than at $\Phi =$
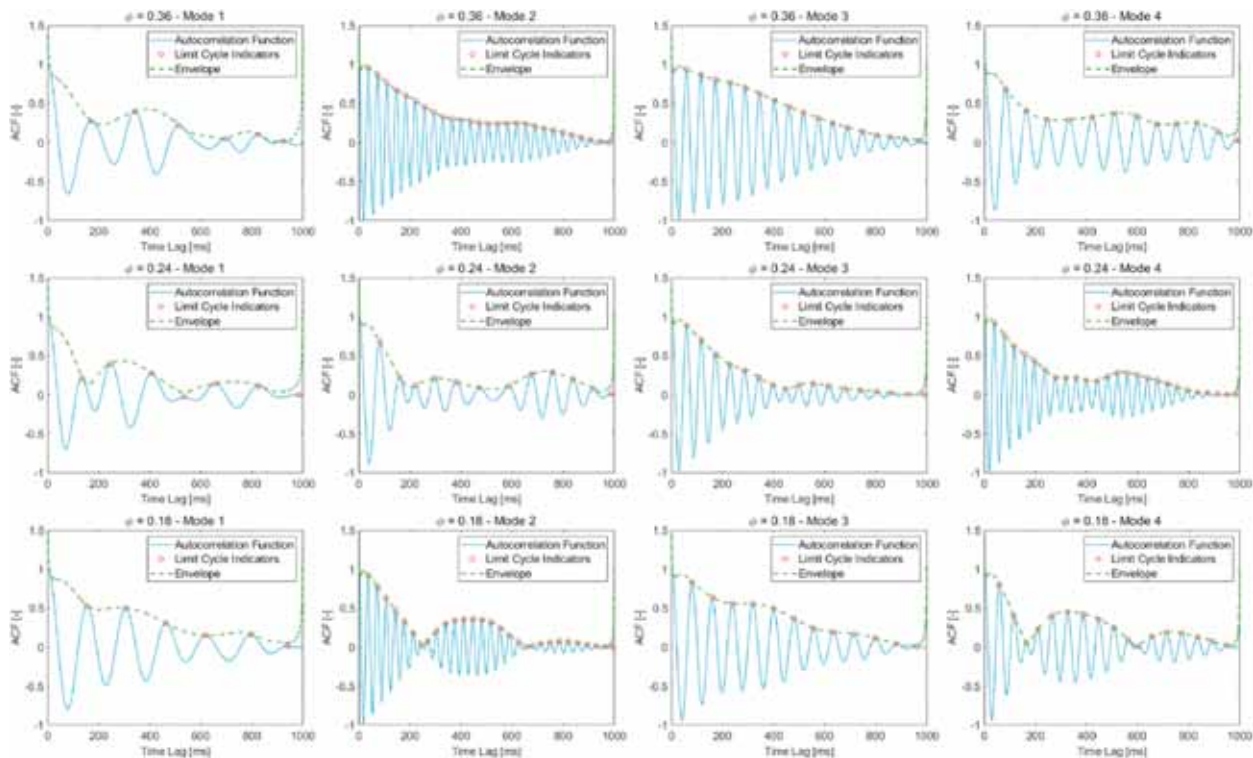

Fig. 27. Autocorrelation function of the mPOD eigenvalues of modes 1–4 at different global equivalence ratio.

0.36. Small, intermittent bursts suggest periods of instability, indicating a transition towards less stable conditions and lean blowout. Finally, at $\Phi = 0.18$ the ACF shows an initial peak followed by rapidly decaying peaks. Significant and frequent bursts with irregular amplitudes indicate high instability and intermittent behavior. The system is highly unstable, with the flame showing clear signs of approaching blowout, as suggested by the rapid decay of the envelope indicating significant damping. These observations highlight the increasing instability of the flame as the system approaches lean blowout conditions.

Fig. 28 provides phase space reconstructions for mode 3 at different global equivalence ratios, offering insights into the dynamic behavior of the system as it transitions through various states. Phase space reconstruction is a powerful technique to visualize the underlying dynamics of a system by plotting the state variable $x(t)$ against the delayed one $x(t + 1)$. At $\Phi = 0.36$, clear, well-defined elliptical orbits indicate regular, periodic behavior with minimal distortion. The system is stable, with consistent and predictable oscillations, suggesting a stable flame condition. Then at $\Phi = 0.24$ slightly distorted elliptical orbits compared to $\Phi = 0.36$ indicate periodic behavior with some irregularities. The increased distortion suggests the system is becoming less stable and transitioning towards quasi-limit cycle behavior, moving towards lean blowout conditions. Finally, at $\Phi = 0.18$ significantly distorted orbits with a spiral-like structure indicate substantial damping and irregular behavior. This pattern is characteristic of a near blowout condition, with flame dynamics dominated by erratic and aperiodic fluctuations, indicating high instability and proximity to blowout.

4. Conclusions

The study analyzes the dynamics of lean swirled Jet-A1 flames using POD, DMD, and mPOD applied to high-speed OH* chemiluminescence images. Data were obtained for lean and ultra-lean flames ($\Phi = 0.36$, $\Phi = 0.24$, and $\Phi = 0.18$) in a 300-kW liquid-fueled swirling combustor.

The analysis involves extrapolating main modal coherent structures and analyzing temporal eigenfunctions and pressure signals. Statistical analysis of pressure signals at $\Phi = 0.36$ and $\Phi = 0.18$ revealed relevant frequencies below 39 Hz, with a 47% decrease in peak under ultra-lean conditions. Wavelet analysis highlighted the increasing relevance of low-frequency components.

Modal analysis involves decomposing modes based on energy content (POD), frequency content (DMD), and both energy and frequency (mPOD). Predominant modes in POD exhibit highest energy, while in mPOD, they correspond to fundamental frequencies. Despite differences between POD and DMD, dominant modes show similarities, with mPOD proving more computationally efficient.

Spatial structures were extracted using POD, followed by FFT analysis of time coefficients to identify frequency content. DMD was used to extract structures at identified frequencies, but images had noisy spatial structures due to single-frequency investigation, unlike mPOD which extracts structures within a frequency range.

As the global fuel-to-air ratio decreases, flame size and intensity diminish while fluctuations increase. Lower equivalence ratios cause the flame to move closer to the injector, transitioning from random to more transitional behavior. Image analysis confirms this trend, with the flame moving closer to the spray zone and luminance variance increasing. Energy in the 1st POD mode increases by about 20% from $\Phi = 0.36$ to $\Phi = 0.18$, indicating dynamic shifts.

FFT of mPOD temporal eigenfunctions reveals dominant frequencies aligning with POD analysis. mPOD efficiently associates spatial structures with frequencies, enhancing understanding of flame dynamics and instability while speeding up calculations. Other techniques (FFT and wavelet decomposition of pressure signals, POD, and DMD) were necessary to characterize the frequency ranges for mPOD filter banks.

The use of mPOD provides a powerful method for characterizing the complex dynamics of Lean Blowout (LBO). By decomposing flow fields into distinct spatial and temporal modes, mPOD enhances resolution and clarity, crucial for identifying precursors to blowout. Isolating coherent structures and filtering out noise, mPOD detects subtle changes in flame behavior, such as intermittent bursts and potential extinction and re-ignition events.

As Φ decreases, the presence and intensity of burst phenomena increase, especially in higher modes, indicating the system's approach to lean blowout. At $\Phi = 0.36$, modes show stable, periodic oscillations without extinction and re-ignition events. However, at lower equivalence ratios ($\Phi = 0.24$ and $\Phi = 0.18$), modes exhibit characteristics indicative of possible flame extinction and re-ignition events. Mode 3 at both $\Phi = 0.24$ and $\Phi = 0.18$, as well as modes 2 and 4 at $\Phi = 0.18$, show bursts starting from zero amplitude or significant amplitude variations, consistent with extinction and re-ignition cycles. These findings highlight the increasing instability of the flame as it approaches lean blowout conditions.

To detect blowout precursors, the nonlinear mPOD eigenvalue time series was also analyzed using the autocorrelation function
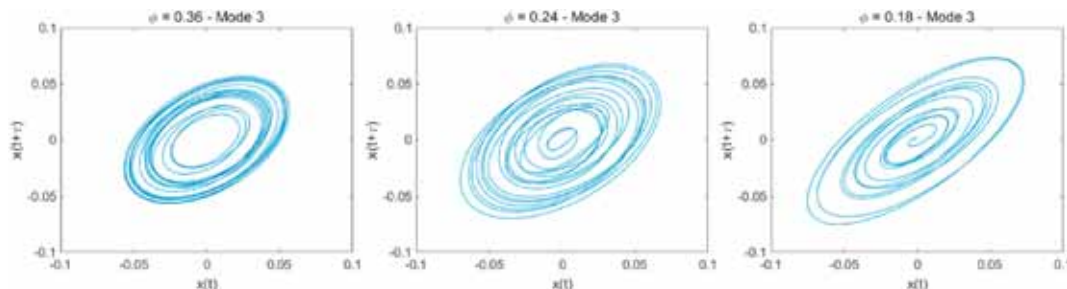

Fig. 28. Phase space reconstruction for the mPOD eigenvalues of mode 3 at different global equivalence ratio.

(ACF) and phase space reconstruction, revealing temporal relationships, periodic behavior, damping, and stability. Burst-like patterns in the ACF indicate intermittent dynamics, crucial for identifying transitions in flame behavior approaching lean blowout conditions. At $\Phi = 0.36$, the ACF shows a strong initial peak followed by gradually decaying peaks, indicating stable periodic behavior and a stable flame. Phase space reconstruction of the mPOD mode 3 eigenvalues shows clear elliptical orbits, confirming regular, periodic behavior and stability. At $\Phi = 0.24$, the ACF displays a strong initial peak with more rapidly decaying subsequent peaks and small, intermittent bursts, suggesting a transition towards less stable conditions. Phase space reconstruction shows slightly distorted elliptical orbits, indicating periodic behavior with some irregularities and a shift towards instability. At $\Phi = 0.18$, the ACF shows an initial peak followed by rapidly decaying peaks with significant and frequent bursts, indicating high instability and intermittent behavior. Phase space reconstruction reveals significantly distorted orbits with a spiral-like structure, characteristic of substantial damping and irregular behavior near blowout conditions. These observations underscore the potential of applying nonlinear time series analysis of mPOD eigenvalues to detect early warning signs of blowout. This approach not only aids in early detection of instability but also improves the understanding of the mechanisms leading to LBO, thereby enhancing predictive capabilities and enabling better control strategies to maintain stable combustion.

Future analysis on nonlinear mPOD eigenvalues time series for detecting precursors to blowout in combustion systems can leverage a variety of advanced techniques. By applying methods such as Lyapunov exponents, recurrence plots, bifurcation analysis, entropy measures, fractal dimension analysis, surrogate data testing, and machine learning, researchers can gain deeper insights into the complex dynamics of flame behavior. These techniques can help identify early warning signs of blowout, allowing for timely interventions to maintain stable combustion and prevent catastrophic failures.

CRediT authorship contribution statement

Maria Grazia De Giorgi: Writing – review & editing, Supervision, Methodology, Conceptualization. **Pasquale Di Gloria:** Writing – original draft, Visualization, Software, Investigation, Formal analysis, Data curation. **Donato Fontanarosa:** Software, Investigation, Formal analysis, Conceptualization. **Antonio Ficarella:** Funding acquisition.

Declaration of competing interest

The authors whose names are listed immediately below certify that they have NO affiliations with or involvement in any organization or entity with any financial interest (such as honoraria; educational grants; participation in speakers' bureaus; membership, employment, consultancies, stock ownership, or other equity interest; and expert testimony or patent-licensing arrangements), or non-financial interest (such as personal or professional relationships, affiliations, knowledge or beliefs) in the subject matter or materials discussed in this manuscript.

We confirm that the manuscript has been read and approved by all named authors and that there are no other persons who satisfied the criteria for authorship but are not listed. We further confirm that the order of authors listed in the manuscript has been approved by all of us. We confirm that we have given due consideration to the protection of intellectual property associated with this work and that there are no impediments to publication, including the timing of publication, with respect to intellectual property. In so doing we confirm that we have followed the regulations of our institutions concerning intellectual property.

We understand that the Corresponding Author is the sole contact for the Editorial process (including Editorial Manager and direct communications with the office). She is responsible for communicating with the other authors about progress, submissions of revisions and final approval of proofs. We confirm that we have provided a current, correct email address which is accessible by the Corresponding Author and which has been configured to accept email from mariagrazia.degiorgi@unisalento.it.

Data availability

Data will be made available on request.

References

[1] Pier Carlo Nassini, Daniele Pampaloni, Roberto Meloni, Antonio Andreini, Lean blow-out prediction in an industrial gas turbine combustor through a LES-based CFD analysis, Combust. Flame 229 (2021) 111391, https://doi.org/10.1016/j.combustflame.2021.02.037. ISSN 0010-2180.

[2] L. Sun, Y. Huang, R. Wang, X. Feng, Z. Liu, J. Wu, FV-MP model to predict lean blowout limits for multi-point lean direct injection combustors, Aero. Sci. Technol. 88 (2019) 185–192, https://doi.org/10.1016/j.ast.2019.03.014.

[3] Achyut Panchal, Suresh Menon, Large eddy simulation of fuel sensitivity in a realistic spray combustor II. Lean blowout analysis, Combust. Flame 240 (2022) 112161, https://doi.org/10.1016/j.combustflame.2022.112161. ISSN 0010-2180.

[4] De Giorgi, Maria Grazia, Aldebara Sciolti, Stefano Campilongo, Antonio Ficarella, Image processing for the characterization of flame stability in a non-premixed liquid fuel burner near lean blowout, Aero. Sci. Technol. 49 (2016) 41–51, https://doi.org/10.1016/j.ast.2015.11.030.

[5] Giorgi De, Maria Grazia, Aldebara Sciolti, Elisa Ficarella Pescini, Antonio, Frequency analysis and predictive identification of flame stability by image processing, Paper No. ES2014-6599, in: ASME 2014 8th International Conference on Energy Sustainability Collocated with the ASME 2014 12th International Conference on Fuel Cell Science, Engineering and Technology, June 30–July 2 2014 V002T04A014, https://doi.org/10.1115/ES2014-6599. Boston, Massachusetts, USA.

[6] Qianpeng Zhao, Jinhu Yang, Cunxi Liu, Shaolin Wang, Yong Mu, Gang Xu, Junqiang Zhu, Lean blowout characteristics of spray flame in a multi-swirl staged combustor under different fuel decreasing rates, Chin. J. Aeronaut. 35 (12) (2022) 130–143, https://doi.org/10.1016/j.cja.2022.06.008. ISSN 1000-9361.

[7] Dae Jin Jang, Min Chul Lee, Evaluating the adequacy of dynamic pressure remote sensing method in a model gas turbine combustor, Case Stud. Therm. Eng. 36 (2022) 102184, https://doi.org/10.1016/j.csite.2022.102184. ISSN 2214-157X.

[8] L. Zheng, R. Boylu, J. Cronly, I. Ahmed, E. Ubogu, B. Khandelwal, Experimental study on the impact of alternative jet fuel properties and derived cetane number on lean blowout limit, Aeronaut. J. 126 (1306) (2022) 1997–2016, https://doi.org/10.1017/aer.2022.33.

[9] Yuxuan Zhang, Xiaomin He, Jintao Wang, Fei Zhang, Yudong Kang, Ignition, lean blowout, and flame propagation in a combustor using flameholder with a trapped vortex cavity, Fuel 324 (Part B) (2022) 124656, https://doi.org/10.1016/j.fuel.2022.124656. ISSN 0016-2361.

[10] Veeraraghava Raju Hasti, Abhishek Navarkar, Jay P. Gore, A data-driven approach using machine learning for early detection of the lean blowout, Energy and AI 5 (2021) 100099, https://doi.org/10.1016/j.egyai.2021.100099. ISSN 2666-5468.

[11] B. Begiashvili, N. Groun, J. Garicano-Mena, S. Le Clainche, E. Valero, Data-driven modal decomposition methods as feature detection techniques for flow problems: a critical assessment, Phys. Fluids 35 (4) (2023) 041301, https://doi.org/10.1063/5.0142102. ISSN 1070-6631.

[12] Can Ruan, Feier Chen, Weiwei Cai, Yong Qian, Liang Yu, Xingcai Lu, Principles of non-intrusive diagnostic techniques and their applications for fundamental studies of combustion instabilities in gas turbine combustors: a brief review, Aero. Sci. Technol. 84 (2019) 585–603, https://doi.org/10.1016/j.ast.2018.10.002.

[13] A.G. Charalambides, S. Sahu, Y. Hardalupas, A.M.K.P. Taylor, Y. Urata, Evaluation of homogeneous Charge compression ignition (HCCI) autoignition development through chemiluminescence imaging and proper orthogonal decomposition, Appl. Energy 210 (2018) 288–302, https://doi.org/10.1016/j.apenergy.2017.11.010.

[14] Tao Zhou, Kai Zhao, Feng Li, Kefu Wang, Nan Meng, Duo Wang, Effects of swirl numbers on the unsteady characteristics of pilot flame in a triple-swirler staged combustor, Case Stud. Therm. Eng. 44 (2023) 102846, https://doi.org/10.1016/j.csite.2023.102846. ISSN 2214-157X.

[15] Zhaoyi Xu, Yanjie Guo, Joseph Homer Saleh, Multi-objective optimization for sensor placement: an integrated combinatorial approach with reduced order model and Gaussian process, Measurement 187 (2022) 110370, https://doi.org/10.1016/j.measurement.2021.110370. ISSN 0263-2241.

[16] Weijie Liu, Ranran Xue, Liang Zhang, Qian Yang, Huiru Wang, Nonlinear response of a premixed low-swirl flame to acoustic excitation with large amplitude, Combust. Flame 235 (2022) 111733, https://doi.org/10.1016/j.combustflame.2021.111733. ISSN 0010-2180.

[17] Donato Fontanarosa, Maria Grazia De Giorgi, Giuseppe Ciccarella, Elisa Pescini, Antonio Ficarella, Combustion performance of a low NOx gas turbine combustor using urea addition into liquid fuel, Fuel 288 (2021), https://doi.org/10.1016/j.fuel.2020.119701. ISSN 0016-2361.

[18] Maria Grazia De Giorgi, Donato Fontanarosa, Antonio Ficarella, Elisa Pescini, Effects on performance, combustion and pollutants of water emulsified fuel in an aeroengine combustor, Appl. Energy 260 (2020), https://doi.org/10.1016/j.apenergy.2019.114263. ISSN 0306-2619.

[19] Zhen Cao, Y.U. Xin, Jiangbo Peng, H.U. Bin, Zhonghao Wang, Y.U. Yang, Long Gao, Minghong Han, Xun Yuan, W.U. Guohua, Flame features and oscillation characteristics in near-blowout swirl-stabilized flames using high-speed OH-PLIF and mode decomposition methods, Chin. J. Aeronaut. 36 (1) (2023) 191–200, https://doi.org/10.1016/j.cja.2022.05.009. ISSN 1000-9361.

[20] Rajasegar R., Choi J., McGann B., Oldani A., Lee T., Hammack S.D., Carter C.D., Yoo J., Comprehensive Combustion Stability Analysis Using Dynamic Mode Decomposition. Energy & Fuels, 0887–0624, https://doi.org/10.1021/acs.energyfuels.8b02433.

[21] L. Weixuan, Z. Dan, Z. Linqing, C. Xiong, Proper orthogonal and dynamic mode decomposition analyses of nonlinear combustion instabilities in a solid-fuel ramjet combustor, Therm. Sci. Eng. Prog. 27 (2022), https://doi.org/10.1016/j.tsep.2021.101147. ISSN 2451-9049.

[22] Paul Palies, Ragini Acharya, Flame-resolved transient simulation with swirler-induced turbulence applied to lean blowoff premixed flame experiment, Combust. Flame 226 (2021) 14–30, https://doi.org/10.1016/j.combustflame.2020.011.041. ISSN 0010-2180.

[23] Yuvi Nanda, Ephraim Gutmark, Modal analysis of combustion instabilities in interacting swirl nozzles, AIAA Scitech 2021 Forum 11–15 (January 2021) 19–21, https://doi.org/10.2514/6.2021-0792.

[24] P. Palies, D. Davis, R.K. Cheng, M. Ilak, Dynamic mode decomposition (DMD) application to premixed low swirl injector flames, in: 68th Annual Meeting of the APS Division of Fluid Dynamics, Monday November 23 2015. Boston.

[25] Fan Yang, Tao Wu, Hui Jiang, Jinyang Jiang, Hao Hanxue, Lianqiang Zhang, A new method for transformer hot-spot temperature prediction based on dynamic mode decomposition, Case Stud. Therm. Eng. 37 (2022) 102268, https://doi.org/10.1016/j.csite.2022.102268. ISSN 2214-157X.

[26] M.A. Mendez, D. Hess, B.B. Watz, J.-M. Buchlin, Multiscale proper orthogonal decomposition (mPOD) of TR-PIV data—a case study on stationary and transient cylinder wake flows, Meas. Sci. Technol. 31 (2020), https://doi.org/10.1088/1361-6501/ab82be.

[27] Miguel Mendez, Mikhael Balabane, Jean-Marie Buchlin, Multi-scale proper orthogonal decomposition (mPOD), AIP Conf. Proc. 1978 (2017), https://doi.org/10.1063/1.5043720.

[28] A. Procacci, M.M. Kamal, M.A. Mendez, S. Hochgreb, A. Coussement, A. Parente, Multi-scale proper orthogonal decomposition analysis of instabilities in swirled and stratified flames, Phys. Fluids 34 (2022) 124103, https://doi.org/10.1063/5.0127956.

[29] Wenkai Shen, Chang Xing, Li Liu, Qiming Hu, Guohua Wu, Yujia Yang, Shaohua Wu, Penghua Qiu, Jiangquan Wu, Chemiluminescence-based characterization of heat release rate dynamic in a micro gas turbine combustion chamber, J. Energy Inst. 102 (2022) 32–41, https://doi.org/10.1016/j.joei.2022.01.006. ISSN 1743-9671.

[30] Yao Liu, Jianguo Tan, Zhengwang Gao, Taiyu Wang, Minggang Wan, Experimental investigation of chemiluminescence and NOx emission characteristics in a lean premixed dual-swirl flame, Case Stud. Therm. Eng. 28 (2021) 101653, https://doi.org/10.1016/j.csite.2021.101653. ISSN 2214-157X.

[31] J. Tobias, D. Depperschmidt, C. Welch, R. Miller, M. Uddi, A.K. Agrawal, R. Daniel Jr., OH* chemiluminescence imaging of the combustion products from a methane-fueled rotating detonation engine, ASME. J. Eng. Gas Turbines Power 141 (2) (October 4 2018) 021021, https://doi.org/10.1115/1.4041143. February 2019.

[32] Yogesh Aradhey, Chuchen Li, Joseph Meadows, Coupled droplet dynamics: investigation of acoustic-spray interactions in a reacting flow field, Combust. Flame 250 (2023) 112645, https://doi.org/10.1016/j.combustflame.2023.112645. ISSN 0010-2180.

[33] Mengmeng Zhao, David Buttsworth, Rishabh Choudhury, Experimental and numerical study of OH* chemiluminescence in hydrogen diffusion flames, Combust. Flame 197 (2018) 369–377, https://doi.org/10.1016/j.combustflame.2018.08.019. ISSN 0010-2180.

[34] G. Thampi, R.I. Sujith, Intermittent burst oscillations: signature prior to flame blowout in a turbulent swirl-stabilized combustor, J. Propul. Power 31 (6) (2015) 1661–1671.

[35] Vishnu R. Unni, R.I. Sujith, Flame dynamics during intermittency in a turbulent combustor, Proc. Combust. Inst. 36 (3) (2017) 3791–3798, https://doi.org/10.1016/j.proci.2016.08.030.

[36] V. Nair, G. Thampi, R.I. Sujith, Intermittency route to thermoacoustic instability in turbulent combustors, J. Fluid Mech. 756 (Oct. 2014) 470–487, https://doi.org/10.1017/jfm.2014.468.

[37] A. Lozano-Durán, O. Flores, J. Jiménez, The three-dimensional structure of momentum transfer in turbulent channels, J. Fluid Mech. 694 (2012) 100–130, https://doi.org/10.1017/jfm.2011.524.

[38] l. Sirovich, Turbulence and the dynamics of coherent structures part iii: dynamics and scaling, Q. Appl. Math. 45 (3) (1987) 583–590. Retrieved from, http://www.jstor.org/stable/43637459.

[39] C. Tropea, A.L. Yarin, J.F. Foss, Springer Handbook of Experimental Fluid Mechanics, vol. 1, Springer Science & Business Media, 2007.

[40] A.M. Kypraiou, A.P. Dowling, E. Mastorakos, N. Karimi, Proper orthogonal decomposition analysis of a turbulent swirling self-excited premixed flame. https://doi.org/10.2514/6.2015-0425, 2015.

[41] J.L. Lumley, The structure of inhomogeneous turbulence, Atmospheric Turbulence and Wave Propagation (1967) 166–178. AM Yaglom, VI Tatarski.

[42] Mihailo R. Jovanović, Peter J. Schmid, Joseph W. Nichols, Sparsity-promoting dynamic mode decomposition, Phys. Fluids 26 (2) (2014) 024103, https://doi.org/10.1063/1.4863670.

[43] M.A. Mendez, M. Balabane and J.-M. Buchlin. Multi-Scale Proper Orthogonal Decomposition of Complex Fluid Flows. DOI: 10.1017/jfm.2019.212.

[44] I. Daubechies, Ten Lectures on Wavelets, SIAM, Philadelphia, PA, USA, 1992.

[45] Y.-F. Sang, D. Wang, J.-C. Wu, Entropy-based method of choosing the decomposition level in wavelet threshold de-noising, Entropy 12 (6) (2010) 1499–1513, https://doi.org/10.3390/e12061499.

[46] C.E. Shannon, A mathematical theory of communication, Bell System Technical Journal 27 (3) (July 1948) 379–423, https://doi.org/10.1002/j.1538-7305.1948.tb01338.x.

[47] Can Ruan, Feier Chen, Tao Yu, Weiwei Cai, Xinling Li, Xingcai Lu, Experimental characterization of flame/flow dynamics during transition between stable and thermo-acoustically unstable conditions in a gas turbine model combustor, Aero. Sci. Technol. 102 (2020) 105858, https://doi.org/10.1016/j.ast.2020.105858. ISSN 1270-9638.

[48] S. Terhaar, K. Oberleithner, C. Paschereit, Key parameters governing the precessing vortex core in reacting flows: an experimental and analytical study, Proc. Combust. Inst. 35 (3) (2015) 3347–3354.

[49] R. Sadanandan, Aritra Chakraborty, Vinoth Kumar Arumugam, Satyanarayanan Chakravarthy, Transition between Swirl and Bluffbody Flame Stabilization in a Novel Ultra-lean Non-premixed Burner, 2017.

[50] Tongxun Yi, Domenic A. Santavicca, Combustion instability and flame structure of turbulent swirl-stabilized liquid-fueled combustion, J. Propul. Power 28 (5) (2012) 1000–1014.

[51] Chi Zhang, Chao Tao, Heng Song, Xiao Han, Li Lei, Xunchen Liu, Fei Qi, Experimental investigations on central vortex core in swirl spray flames using high-speed laser diagnostics, Phys. Fluids 35 (3) (2023) 035130, https://doi.org/10.1063/5.0141795.

[52] P.M. Morse, H. Feshbach, Methods of Theoretical Physics, vol. 1, McGraw-Hill, New York, 1953.